MAGNETIC AC SUSCEPTIBILITY, MAGNETIC FLUX MAPPING, AND CURRENT DISTRIBUTIONS IN HIGH TEMPERATURE THIN-FILM SUPERCONDUCTORS

by

Weibing Xing
B.Sc., Ningxia University, 1982
M.Sc., Simon Fraser University, 1990

THESIS SUBMITTED IN PARTIAL FULFILLMENT OF
THE REQUIREMENTS FOR THE DEGREE OF
DOCTOR OF PHILOSOPHY

in the Department
of
PHYSICS

SIMON FRASER UNIVERSITY
April 1995

Approval

Name: Weibing Xing

Degree: Doctor of Philosophy (Physics)

Title of thesis: Magnetic ac susceptibility, magnetic flux mapping, and current distributions in high temperature thin-film superconductors

Examining Committee:
Chair: Jeffrey R. Dahn

Bret Heinrich
Senior Supervisor

Anthony S. Arrott

Suso Gygax

Chuck Irwin

Albert Curzon
Internal Examiner

Ron B. Goldfarb
External Examiner
NIST, Boulder, Colorado, U.S.A.

Date Approved: 4 April 1995

PARTIAL COPYRIGHT LICENSE

I hereby grant to Simon Fraser University the right to lend my thesis, project or extended essay (the title of which is shown below) to users of the Simon Fraser University Library, and to make partial or single copies only for such users or in response to a request from the library of any other university, or other educational institution, on its own behalf or for one of its users. I further agree that permission for multiple copying of this work for scholarly purposes may be granted by me or the Dean of Graduate Studies. It is understood that copying or publication of this work for financial gain shall not be allowed without my written permission.

Title of Thesis/Project/Extended Essay

Magnetic ac susceptibility, magnetic flux mapping, and current distributions in high temperature thin-film superconductors.

Author: _____
(signature)

Weibing Xing
(name)

April , 1995
(date)

Abstract

The complex ac susceptibilities, $\chi = \chi' - i\chi''$, of thin films of the high temperature superconductors (HTS) $YBa_2Cu_3O_{7-\delta}$ (YBCO) and Tl-Ba-Ca-Cu-O (TBCCO) have been studied as functions of temperature, driving field amplitude, and ac frequency. The temperature and field dependences of the measured ac susceptibilities were found to be in good agreement with model calculations. The peak positions of χ'' were used to determine the temperature-dependent critical current density $j_c(T)$. Values of the critical current densities were between those obtained by inductive and magnetic flux mapping techniques. It was found that the ac susceptibilities of HTS thin films depend weakly on the frequency of the applied field. The frequency-dependent χ'' peak temperature, $T_p(f)$, was interpreted with a model based on thermally activated flux creep.

Magnetic flux densities normal to the film plane for rectangular HTS thin films were mapped by means of a scanning micro-Hall probe (25×25 μm active area). The applied fields were oriented perpendicular to the film surface, along the z axis. The flux density maps, $B_z(x,y)$, for uniform thin-film samples showed patterns which reflect the symmetry of the sample geometry. An inverse calculation algorithm was developed to convert the measured B_z maps into thin-film sheet magnetization maps and sheet current maps. The inverse calculations showed that the sheet currents are always present over the entire sample, including the vortex-free region. The sheet currents reach the critical values in the vortex-penetrated regions. In the vortex-free regions the sheet currents are unsaturated. The critical sheet currents tend to follow the sample edges. This sheet current distribution explains the effective shielding or trapping of the magnetic flux along the film diagonals. The unsaturated sheet currents along the virgin path of the hysteresis loop circulate in round loops; after the field reverses its direction the unsaturated sheet currents follow multiply-connected patterns. It

is shown that the multiply-connected current patterns can be reconstructed from the superposition of two appropriate initial current distributions obtained along the virgin path. The critical current density was found to depend on local magnetic flux density, and it follows the Kim model. The sheet current was also found to be very sensitive to defects in the films.

From the known sheet current distributions, the spatial distributions of the total flux density $\mathbf{B}(x,y,z)$, including the tangential components $B_{x,y}(x,y,z)$, were calculated in the vicinity of the thin-film samples. The total flux distributions allow one to visualize the flux behavior in various vortex states for HTS thin-film superconductors. The quantitative information obtained by the inductive and flux mapping techniques has proven useful in optimizing the deposition conditions for HTS thin films for further device applications.

Acknowledgments

First, I would like to thank my senior supervisor, Prof. Bret Heinrich, for his tireless guidance, inspiration, and financial support during my Ph.D. study. Prof. Heinrich has shared with me the excitement associated with the new experimental results and ideas that emerged during our many lengthy discussions. I have benefited and learned a great deal from his knowledge, wisdom, and intuition of physics. The freedom he gave to me in the laboratory allowed me to gain valuable experience in building experimental apparatus and in conducting independent research.

The work carried out in this thesis was a part of a collaborative program involving groups at Simon Fraser University, the University of British Colombia, and CTF Systems. I would like to express my thanks to my colleagues, Dr. Sergej Govorkov, Per Brown, and Dr. Janusz Chrzanowski for very valuable technical assistance and discussions during our collaborative effort.

My work has been helped greatly by having access to a wide range of structural studies which were performed by Prof. Chuck Irwin's and Prof. Albert Curzon's groups.

I would like to express my sincere thanks to Prof. Suso Gygax for introducing me to the field of superconductivity. The training provided by him has been very useful in carrying out the present work.

I feel very honored to have Prof. Anthony Arrott to be a member of my supervisory committee. I always admire his wisdom, sharp thinking, and deep insight about physics.

I gratefully acknowledge Dr. Ilya Entin and Peter Grant of the National Research Council, Ottawa, for helpful discussions.

I am indebted to Dr. Ron Goldfarb of the National Institute of Standards and Technology, Boulder, Colorado, for his careful reading of our published manuscripts and fruitful discussions.

I am grateful to Dr. Al Fife, Dr. Hu Zhou, and Alan Cragg of CTF Systems Inc. for the constant supply of samples, for various forms of technical support, and for helpful suggestions which were very beneficial in writing my thesis and papers. I appreciate the opportunity of working with them on an industrial project. The work presented in this thesis would not have been possible without their support.

I would like to express my many thanks to Ken Myrtle, David Atlan, and Dr. Jae-Gwang Lee for their help with various technical details.

Finally, I gratefully acknowledge the financial support of NCERC, Industry Canada (STP-AIM program), and the B.C. Minister of Employment and Investment, during this thesis study.

Table of Contents

List of Tables

List of Figures

Chapter 1
Introduction

1.1. Introduction

Worldwide research and development on practical applications of high-transition-temperature superconducting (HTS or high-T_c) thin films, for example, the fabrication of superconducting quantum interference devices (SQUIDs) and microwave applications, have spurred studies of the statics and dynamics of vortices in high-T_c thin films at liquid nitrogen temperatures. Such studies are important in both fundamental research and technical applications. AC susceptibility and magnetic flux mapping are two key experimental techniques that have been used for these studies.

The ac susceptibility, including the ac screening technique, probes the dynamic response of vortices in planar superconductors. This technique is very simple and has been widely used for the characterization of superconducting properties of HTS samples [Goldfarb et al. 1987; Gömöry and Lobotka 1988; Clem 1988; Murphy et al. 1989; Chen and Goldfarb 1989]. The measurement of ac susceptibility on HTS thin films is often carried out in a perpendicular configuration in which the applied field is oriented perpendicular to the film surface. This configuration is often encountered in real applications, such as HTS thin-film SQUIDs and transformers. Due to the complex magnetic flux profiles in the perpendicular arrangement, ac susceptibility measurements for HTS thin films remain largely descriptive. Recent progress in theoretical model calculations of magnetic flux profiles and current distributions for the thin-film geometry [Sun et al. 1991; Senoussi 1992; Atsarkin et al. 1992; Mikheenko and Kuzovlev 1993; Zhu et al. 1993; Clem and Sanchez 1994a] has made quantitative study possible,

for example, the determination of critical current densities from the ac susceptibility measurements [Xing et al. 1993, 1994c]. The ac susceptibility can be measured as a function of different experimental parameters, such as temperature, and the amplitude and frequency of the ac driving field. In that way one can gain insight about the dynamic behavior of vortices in the HTS thin films, for example, the influence of thermal activation on the pinning of vortices in the HTS thin-film samples [Nikolo and Goldfarb, 1989; Xing et al. 1994c].

Magnetic flux imaging techniques, such as a scanning Hall probe [Brüll et al. 1991; Rauch et al.; Xing et al. 1994a, 1994b] and magneto-optics [Indenbom et al. 1990; Brüll et al. 1991; Grant et al. 1994; Heinrich et al. 1994], provide quantitative information about the magnetic flux distribution over the HTS thin films. The flux maps can inversely be transformed into sheet magnetization [Xing et al. 1994a, 1994b] which then provides quantitative information about the magnitude and distribution of the critical current density. The investigation of flux and current distributions is important for the characterization of HTS thin films which may be used for further device fabrication. It is well known that the flux noise level observed near a HTS thin film device depends on the critical current density of the film area from which the device is fabricated [Ferrari et al. 1989]. The detailed sheet current distribution can be used to calculate and visualize the three-dimensional spatial distribution of the magnetic flux [Xing et al. 1994c]. Magnetic flux imaging allows one to address fundamental questions concerning the nucleation and propagation of vortices in high-T_c materials. Furthermore, the ability to characterize the superconducting properties on a local scale by non-destructive means is very attractive in device applications based on high-T_c films.

In this thesis, the superconducting properties of high-T_c thin films have been studied by magnetic measurements employing ac susceptometers and a scanning micro-Hall probe. The inductive techniques are very suitable for determining the

critical temperature T_c, and critical current density j_c, over a large area of the sample. Theoretical model calculations of ac susceptibility, for the perpendicular configuration, were summarized and used in the experimental data analysis. The χ'' peak, corresponding to the temperature of maximum loss, was used to estimate the functional dependence of the critical current density on temperature. The ac susceptibility was measured as a function of driving frequencies. The Anderson-Kim flux creep theory [Anderson 1962; Anderson and Kim 1964] was used to model the results.

The scanning micro-Hall probe was used to map the normal component of magnetic flux density (B_z, where z is in the direction normal to the film plane) over the HTS thin-film samples. Patterns of flux trapping and the process of flux nucleation and penetration in the HTS films were obtained in great detail. The scanning Hall probe technique was used as a novel method to determine the distribution of sheet currents in thin-film superconductors. This was achieved by means of inverse calculations which transform the measured flux density maps into sheet magnetizations and sheet current maps. The sheet current patterns were obtained for rectangular thin film geometry. The fully vectorial quantitative studies of the sheet current distribution provided a valuable insight about patterns of the critical and less than critical currents, the field dependence of the critical current, the hysteretic response of critical currents, and the role of sample defects. In addition, the sheet current distribution was employed to determine the magnetic flux density **B** and to visualize the magnetic flux lines around the film.

The inductive and flux mapping techniques are complementary: The simple inductive ac susceptibility measurements were used to select samples with appropriate superconducting transition temperatures before further investigations with the scanning micro-Hall probe were pursued. The scanning Hall probe measurements were very important for the understanding of ac susceptibility

measurements. The susceptibility data are interpreted using simple models describing the flux penetration. The Hall probe measurements allow one to compare the actual flux distribution with that assumed in model calculations of ac susceptibilities; for example, the flux penetration measured by the micro-Hall probe allows one to determine the sample flux penetration at the field which corresponds to the χ'' peak. The critical current was measured by both techniques and the results of these measurements were compared.

1.2. Motivation

This thesis was devoted to the statics and dynamics of vortices in pre-patterned HTS thin films. This work was done as a part of the joint effort among the members of Physics Department, Simon Fraser University; Physics Department, University of British Columbia; and CTF Systems; and Furukawa Electric, Japan. The main effort of this collaboration was aimed towards the development of high-T_c thin-film SQUID magnetometers operated at liquid N_2 temperatures. Fundamentally, these studies were aimed towards the understanding of the magnetic flux penetration, magnetic flux trapping, sheet current distribution, and dynamic response of vortices in HTS thin films. At the same time, these quantitative studies were intended to help CTF Systems to optimize the deposition of HTS thin films and the fabrication of various device patterns. The results obtained during this thesis research have been used by CTF Systems in the development of high-T_c SQUID magnetometers [Fife et al. 1994a, 1994b].

This thesis is organized as follows: Chapter 2 is devoted to the ac susceptibility study, Chapter 3 focuses on the study of flux mapping and current distributions using the scanning micro-Hall probe technique, and Chapter 4 demonstrates spatial distributions of the total flux density in the vicinity of a thin-film sample.

Chapter 2
AC Susceptibility Study

2.1. Introduction

The ac susceptibility technique has been used widely for characterizing high temperature superconductors. In addition to its use for the determination of the critical temperature and magnetic penetration depth [Xing 1990], the ac susceptibility technique has been employed to determine the critical current densities of sintered high temperature superconductors [Murphy et al. 1989; Gömöry and Lobotka 1988; Chen and Goldfarb 1989; Clem 1988]. The determination of j_c by an inductive method has many advantages over the usual transport measurement. First, it needs no sample processing, for example, defining a narrow strip and attaching current and voltage leads. Second, the inductive measurement is nondestructive; therefore the sample can be used for further experiments after it has been characterized for critical currents. To avoid demagnetizing effects, the experimental arrangement usually involves slab-shaped samples with the applied magnetic field H_a in the sample plane, or cylindrical samples in an axial field H_a.

For thin-film superconductors, the ac susceptibility measurement presents special problems. First, when the thin films are oriented perpendicular to the applied field, the demagnetization factor D is very close to 1 due to a large sample aspect ratio. Here D is a geometric factor used to give the internal field H = H_a – DM, where H_a is the applied field. In order to obtain the true "internal" susceptibility χ_{int} (defined as dM/dH) from the measured "external" susceptibility χ_{ext} (defined as dM/dH_a), the relation $\chi_{int} = \chi_{ext}/(1-D\chi_{ext})$ is used [Goldfarb 1986]. A large demagnetization correction has to be made, and the conversion

may result in divergent behavior [Goldfarb et al. 1992]. Secondly, the large demagnetization effect in thin-film samples results in complicated magnetic flux profiles (see discussions in Chapters 3 and 4). Consequently, the solution of the Maxwell equation, $\nabla \times \mathbf{H} = \mathbf{j}$, involves a great effort in either numerical or analytical methods, and the interpretation of ac susceptibility measurements is largely limited to empirical descriptions. Moreover, when the thin film is oriented parallel to the applied field ($D \approx 0$ and $\chi_{int} \approx \chi_{ext}$), parallel configuration, the measured signal is very weak and difficult to detect, because of the small areas of the current paths. The problem becomes even more pronounced when the thickness of the thin film is comparable to the penetration depth. Since perfect magnetic flux exclusion cannot be achieved, the measured signal is further reduced. In reality, the parallel alignment of the film is very difficult to achieve, because even small deviations from parallel yield an enhanced χ_{ext} which must be analyzed with an effective demagnetization factor close to 1 in order to yield a meaningful χ_{int}. Therefore, it is preferable to measure the thin films in the perpendicular orientation.

Theoretical calculations of magnetic flux distributions in thin-film superconductors have been carried out by many authors. Frankel [1979] first calculated the spatial distribution of the axial flux density in a disk-shaped superconductor, using an iterative procedure. Däumling and Larbalestier [1989] used finite element analysis and extended the numerical calculation to including radial component of the flux density generated by the screening currents. The calculations demonstrated complicated magnetic flux profiles. The conclusions showed that when the amplitude of an applied field H_a reaches the value of the characteristic field $H^* \sim j_c d$, where d is the disk thickness, the flux nearly penetrates to the center of the sample. This was validated by magnetic and

resistive measurements on disk-shaped Nb_3Sn specimens [Däumling and Larbalestier 1989].

Analytical calculations (simplified model) of the hysteretic diamagnetic moment and the ac susceptibility of disk-shaped superconductors were made by Sun [1989], Sun et al. [1991], Senoussi [1992], and Atsarkin et al. [1992]. These calculations were based on the assumption that the current is critical in the vortex-penetrated region and zero elsewhere. This is a crude assumption as we now know from our experimental observations. However, the calculations have provided reasonable fits for the ac susceptibilities of HTS thin films [Atsarkin et al. 1992; Xing et al. 1993].

Recently, more sophisticated, realistic, theoretical calculations of magnetic flux and current distributions and ac susceptibilities for type-II disc superconductors in perpendicular configuration were carried out by Mikheenko and Kuzovlev [1993], Zhu et al. [1993], and Clem et al. [1994a]. The calculations are based on the assumption that the term ($= 2B_{x,y}/d$) due to the curvature of the flux density **B** (i.e. the curvature of the flux line) in Ampere's law is the dominating term which determines the currents (see Clem 1994b and Chapter 4). Here $B_{x,y}$ is the tangential (parallel) component of **B**. The consequence of this assumption is that the current is distributed over the whole sample including the vortex-free region. This prediction is in agreement with our experimental observations [Xing et al. 1994a, 1994b].

This chapter presents the temperature dependent, complex ac susceptibilities of $YBa_2Cu_3O_{7-\delta}$ (YBCO) thin films prepared by the laser ablation technique. The applied ac fields were perpendicular to the film surface. The fundamental frequency component of the ac susceptibility was measured. The measured ac susceptibilities were used for the evaluation of the critical current densities as a function of T, $j_c(T)$. The measured susceptibilities as a function of temperature

and $j_c(T)$ resemble closely those which were obtained by model calculations and that allowed one to interpret quantitatively the measured data. The measured $j_c(T)$ relations were compared to those obtained at CTF using an ac screening technique. The j_c values estimated by the inductive methods were compared with those of the scanning Hall probe measurement [Xing et al. 1994a]. The $j_c(T)$ was found to be weakly dependent on the frequency of the ac driving field and this behavior was interpreted by using a scaling argument [Malozemoff et al. 1988] based on the Anderson-Kim flux creep theory [Anderson 1962; Anderson and Kim 1964].

2.2. Theoretical calculations

2.2.1. General formulas

In response to a perpendicularly applied external field H_a, a type-II thin-disc (thin-film) superconductor induces shielding currents to exclude the magnetic flux from its interior. These supercurrents are associated with the diamagnetic magnetization **M** [Jackson 1975],

$$\mathbf{M} = \frac{1}{2V}\int_{V'} \mathbf{x}' \times \mathbf{j}(\mathbf{x}')\, d^3x', \tag{2.1}$$

where $V = \pi R^2 d$ is the disc volume, R the radius of the disk, and d the disc thickness. **M** has only the axial (z) component, $M \cdot \hat{z}$. The current distribution j(x,y) is determined from the magnetic flux distribution inside the specimen (Ampere's law). For an ac excitation field

$$H_a(t) = H_0 \sin \omega t, \tag{2.2}$$

M is a function of time, M(t).

The internal field H_{in} of the thin-film sample is enhanced by the demagnetization effect, $H_{in} \approx H_a/(1 - D)$. If H_{in} exceeds the lower critical field H_{c1}, the thin-film superconductor transforms into a mixed (vortex) state and its magnetic response becomes nonlinear due to the flux pinning effect. The magnetization induced by the sinusoidal field traverses a minor hysteresis loop and can be expressed by a Fourier series [Ishida and Goldfarb 1990],

$$M(t) = H_0 \sum_{n=1}^{\infty} \left(\chi_n' \sin n\omega t - \chi_n'' \cos n\omega t \right), \tag{2.3}$$

where $\chi_n = \chi_n' - i\chi_n''$ is the nth harmonic of ac susceptibility, and χ_n' and χ_n'' are the real (in-phase) and imaginary (out-of-phase) parts of χ_n, respectively.

The fundamental frequency component of the ac susceptibility (n = 1), $\chi = \chi' - i\chi''$, for type-II superconductors has clear physical meanings: χ' corresponds to the dispersive magnetic response, reflecting the supercurrent shielding effect; χ'' corresponds to energy dissipation, reflecting the hysteretic loss. For example, for a thin-film superconductor, the loss per cycle per unit volume, W_v, is [Clem and Sanchez 1994a]

$$W_v = \mu_0 \oint H_a dM = \mu_0 \pi H_0^2 \chi''. \tag{2.4}$$

The in-phase and out-of-phase ac susceptibilities are given by the Fourier coefficients in Eq. (2.3),

$$\chi_n' = \frac{1}{\pi H_0} \int_0^{2\pi} M(t) \sin(n\omega t) d(\omega t), \tag{2.5a}$$

and $$\chi_n'' = -\frac{1}{\pi H_0}\int_0^{2\pi} M(t)\cos(n\omega t)d(\omega t). \qquad (2.5b)$$

The ac response of the thin-film sample can be measured with a susceptometer described in Sec. 2.3. The voltage detected by a lock-in amplifier (referenced to the fundamental frequency) has two components: the in-phase voltage $v' \propto \omega H_0\chi'$, and the out-of-phase voltage $v'' \propto \omega H_0\chi''$. The proportionality constant is an instrumental scaling factor which can be determined by calibration procedures [Goldfarb and Minervini 1984].

2.2.2. Simplified approach

The simplified approach [Senoussi 1992; Atsarkin et al. 1992; Sun 1989; Sun et al. 1991] assumes that the shielding currents are induced at sample edges when a zero-field-cooled thin disc superconductor is exposed to a weak magnetic field H_a perpendicular to the disk surface, see Fig. 2.1. For increasing H_a, the currents propagate towards the film center. At the disk center ($\mathbf{x} = 0$), the applied flux density $B_a = \mu_0 H_a$ is completely compensated by the self-induction $\mathbf{B}_{self}$ of the shielding currents flowing in an annulus of the disk. $\mathbf{B}_{self}$ is given by [Jackson 1975]

$$\mathbf{B}_{self}(\mathbf{x}=0) = \frac{\mu_0}{4\pi}\int_V \frac{\mathbf{j}\times\mathbf{x}'}{|\mathbf{x}'|^3} d^3x'. \qquad (2.6)$$

By symmetry, $\mathbf{B}_{self}(\mathbf{x} = 0)$ is along the axial direction (opposite the direction of B_a). Equation (2.6) defines a radius, r*, for the flux penetration in an applied field H_0,

$$r^* = R\, e^{-2h/3}, \tag{2.7}$$

where $h = H_0/H^*$ is the reduced field, and $H^* = j_c d/3$ is the characteristic field. The supercurrents reach the critical values within $r^* < r < R$.

Combining Eqs. (2.3) and (2.6) gives the initial increase in magnetization (H_a increases from zero to $H_0 \geq 0$)

$$M_{ini}(H_a) = -M_{sat}\left(1 - e^{-2H_a/H^*}\right), \tag{2.8}$$

and the hysteretic magnetization

$$M^{\pm}(H_a) = \mp M_{sat}\left(1 + e^{-2h} - 2e^{-h(1 \pm H_a/H_0)}\right), \tag{2.9}$$

where $M_{sat} = j_c R/3$, and the $\pm$ sign in $M^{\pm}$ stands for increasing (+) and decreasing (-) applied fields, respectively. The initial and the hysteretic magnetizations as functions of the applied field are plotted in Fig. 2.2 (dashed lines). In Fig. 2.2, we have assumed $j_c = 3 \times 10^6$ A/cm^2, $d = 3 \times 10^{-5}$ cm, and $\mu_0 H_0 = 12$ mT. M has the following asymptotic behavior:

$$\left.\begin{aligned} M_{ini} &\approx -\chi_0 H_a \\ M^{\pm} &\approx \mp \chi_0 H_a \end{aligned}\right\} \quad \text{for } h \ll 1, \tag{2.10a}$$

$$\left.\begin{aligned} M_{\text{int}} &\approx -M_{sat} \\ M^{\pm} &\approx \mp M_{sat} \end{aligned}\right\} \quad \text{for } h \gg 1, \tag{2.10b}$$

where $\chi_0 = 2R/d$. Therefore, $-\chi_0$ represents the complete diamagnetic susceptibility for weak external fields, and M_{sat} represents the saturation magnetization for strong external fields. It is interesting to note that $M_{sat} = j_c R/3$

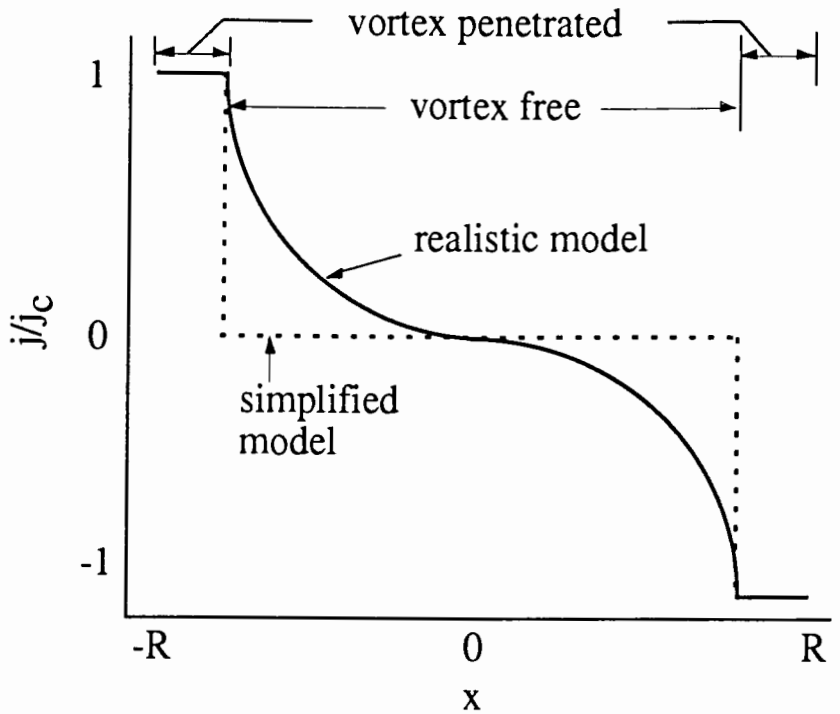

Fig. 2.1. Schematics of current density profiles for simplified (dashed lines) and realistic (solid lines) models.

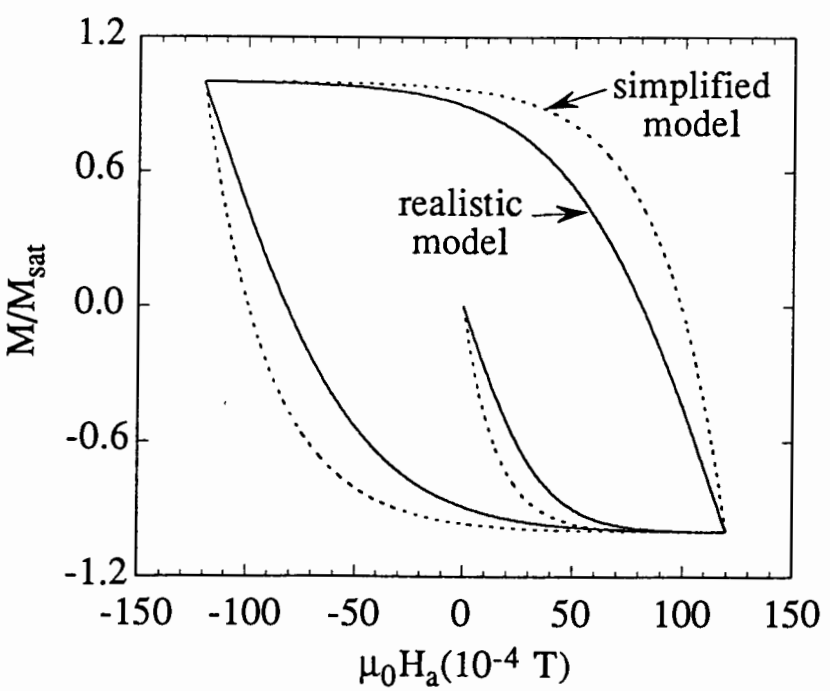

Fig. 2.2. Initial and hysteretic magnetizations as functions of the applied field for simplified (dashed lines) and realistic (solid lines) models.

is the same as that of a long cylinder of radius R in an axial external field [Bean 1962]. The numerical calculations of Frankel [1978] and Däumling and Larbalestier [1989] also gave the same M_{sat}.

For the ac excitation field (2.2), Eq. (2.9) becomes

$$M^{\pm}(t) = \mp M_{sat}\left(1 + e^{-2h} - 2e^{-h(1\pm\sin\omega t)}\right). \tag{2.11}$$

Substituting M(t) into Eq. (2.5), we have

$$\chi'(h) = -\chi_0 \frac{2\, I_1(h)\, e^{-h}}{h}, \tag{2.12a}$$

and $$\chi''(h) = 2\chi_0 \frac{h - 1 + (h+1)e^{-2h}}{\pi h^2}, \tag{2.12b}$$

where I_1 is the first-order modified Bessel function. Since $h = H_0/H^*$ and $H^* = j_c(T)d/3$, χ' and χ'' in Eq. (2.12) are implicit functions of the amplitude H_0 of an applied field and temperature T. χ', and χ'' have the following asymptotic behavior:

$$\left.\begin{aligned} \chi' &\approx -\chi_0 \\ \chi'' &\approx 1.27\chi_0 h \end{aligned}\right\} \quad \text{for } h \ll 1, \tag{2.13a}$$

$$\left.\begin{aligned} \chi' &\approx -0.80\chi_0 h^{-3/2} \\ \chi'' &\approx 0.64\chi_0 h^{-1} \end{aligned}\right\} \quad \text{for } h \gg 1. \tag{2.13b}$$

Figure 2.3(a) shows the plots of the calculated χ' and χ'' as functions of h. Experimentally, χ' and χ'' are either functions of temperature T or of the applied

field H_a. The numerical calculations show that the χ'' peak position appears at $h = 3H_0/j_c(T)d \approx 1.344$. It follows that

$$\left.\begin{aligned} j_c(T_p) &\approx 3.157 H_{a,rms}/d \\ j_c(T) &\approx 3.157 H_{p,rms}/d \end{aligned}\right\} \quad \text{(SI)}, \tag{2.14a}$$

$$\left.\begin{aligned} j_c(T_p) &\approx 2.512 H_{a,rms}/d \\ j_c(T) &\approx 2.512 H_{p,rms}/d \end{aligned}\right\} \quad \text{(practical units)}, \tag{2.14b}$$

where T_p and $H_{p,rms}$ (rms value) correspond to the peak positions of χ'', and $H_{a,rms}$ ($= H_0/\sqrt{2}$) is in the rms value of the applied field. In the practical units, j_c is in A/cm^2, d in cm, and H_a in Oe. From Eq. (2.7), $r^*(\chi''$ peak$) \approx 0.4R$; that is, the macroscopic flux penetration depth is about 0.6R when χ'' shows a peak.

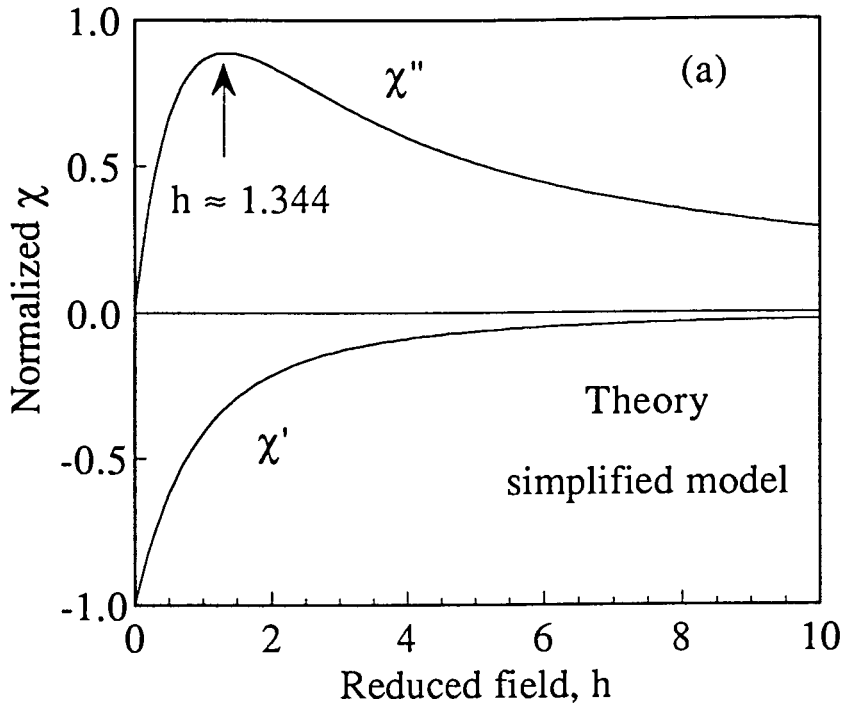

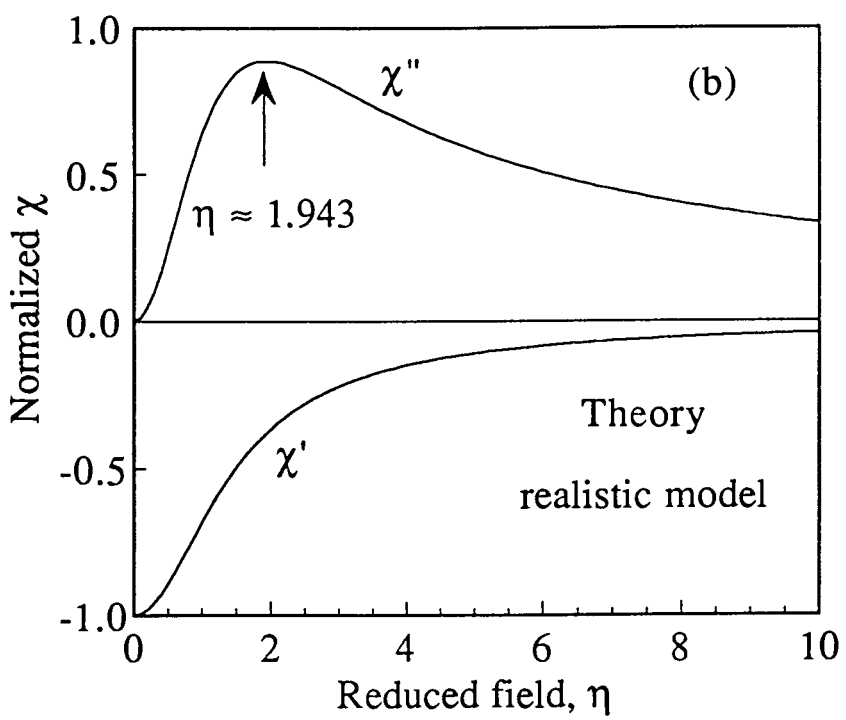

Fig. 2.3. Normalized theoretical χ versus the reduced field for (a) the simplified model (b) the realistic model.

2.2.3. Realistic approach

The realistic approach requires much more complex mathematical treatment. The current distribution includes the shielding currents in the vortex-free region and the critical currents in the vortex-penetrated region [Mikheenko and Kuzovlev 1993; Zhu et al. 1993; Clem and Sanchez 1994a], see Fig. 2.1. For an applied field H_a varying between $-H_0$ and H_0 ($H_0 \geq 0$), $-H_0 \leq H_a \leq H_0$, the initial magnetization M_{ini} and the hysteretic magnetization $M^{\pm}$ are given by

$$M_{ini} = -M_{sat} U(H_a / H^{**}), \tag{2.15}$$

$$M^{\pm}(H_a) = \mp M_{sat}\left[2U\left(\eta_a^{\pm}\right) - U(\eta)\right], \tag{2.16}$$

where $M_{sat} = j_c R/3$, $\eta = H_0/H^{**}$, $H^{**} = j_c d/2$, $\eta_a^{\pm} = \eta(1 \pm H_a/H_0)/2 = (H_0 \pm H_a)/2H^{**}$, and

$$U(x) = \frac{2}{\pi}\left[\cos^{-1}(\operatorname{sech} x) + \tanh x \ \operatorname{sech} x\right]. \tag{2.17}$$

Here η and H^{**} correspond to the reduced and characteristic fields. The initial and the hysteretic magnetizations as functions of the applied field are plotted in Fig. 2.2 (solid lines). The initial macroscopic penetration depth is

$$r^{**} = R / \cosh(\eta). \tag{2.18}$$

Note that $U(x) \approx 4x/\pi$ for $x \ll 1$, and $U(x) \approx 1$ for $x \gg 1$. Therefore, the initial and the hysteretic M have the following asymptotic behavior:

$$\left.\begin{aligned} M_{ini} &\approx -\chi_{00} H_a \\ M^{\pm} &\approx \mp\, \chi_{00} H_a \end{aligned}\right\} \quad \text{for } \eta \ll 1, \tag{2.19a}$$

$$\left.\begin{aligned} M_{ini} &\approx -M_{sat} \\ M^{\pm} &\approx \mp M_{sat} \end{aligned}\right\} \quad \text{for } \eta \gg 1, \tag{2.19b}$$

where $\chi_{00} = 8R/3\pi d$ is the complete screening susceptibility in this case.

For an ac excitation field $H_a(t) = H_0 \sin\omega t$, $\eta_a^{\pm} = \eta(1 \pm \sin\omega t)/2$, and $M^{\pm}(H_a)$ becomes time dependent. Substituting $M^{\pm}(H_a(t))$ into Eq. (2.5), we have

$$\chi'(\eta) = -\chi_{00} \frac{I_{\chi'}(\eta)}{\eta}, \tag{2.20a}$$

and

$$\chi''(\eta) = \chi_{00} \frac{2I_{\chi''}(\eta) - \eta U(\eta)}{\eta^2}, \tag{2.20b}$$

where

$$I_{\chi'}(\eta) = \int_0^{\pi} U(\eta(1+\sin\omega t)/2)\, \sin\omega t\, d(\omega t), \tag{2.21a}$$

and

$$I_{\chi''}(\eta) = \int_0^{\eta} U(x)dx. \tag{2.21b}$$

Apparently, there is no closed solution to integral (2.21a). However, integral (2.21b) can be expressed by some analytical functions plus a polynomial, see Appendix. The asymptotic behavior of χ' and χ'' in (2.20) is given by [Clem and Sanchez 1994a],

$$\left.\begin{aligned} \chi' &\approx -\chi_{00} \\ \chi'' &\approx \chi_{00}\eta^2/\pi \end{aligned}\right\} \quad \text{for } \eta \ll 1, \tag{2.22a}$$

$$\left.\begin{aligned}\chi' &\approx -1.33\chi_{00}\eta^{-3/2}\\ \chi'' &\approx \chi_{00}\eta^{-1}\end{aligned}\right\} \qquad \text{for } \eta \gg 1. \tag{2.22b}$$

Figure 2.3(b) shows plots of χ' and χ'' versus η. Numerically, we found that the χ'' peak appears at $\eta = 2H_0/j_c(T)d \approx 1.943$. Thus, for the realistic approach,

$$\left.\begin{aligned}j_c(T_p) &\approx 1.456 H_{a,rms}/d\\ j_c(T) &\approx 1.456 H_{p,rms}/d\end{aligned}\right\} \qquad \text{(SI)}, \tag{2.23a}$$

$$\left.\begin{aligned}j_c(T_p) &\approx 1.159 H_{a,rms}/d\\ j_c(T) &\approx 1.159 H_{p,rms}/d\end{aligned}\right\} \qquad \text{(practical units)}, \tag{2.23b}$$

The values of the prefactors in (2.23) are about half of those in (2.14). From Eq. (2.18), r**(χ'' peak) $\approx$ 0.3R; that is, the macroscopic flux penetration depth is about 0.7R when χ'' reaches a peak value.

2.2.4. Discussion

Figure 2.3 demonstrates that, except for the χ'' peak position, the overall profiles of the functional dependence of χ' and χ'' on the reduced field are similar for the two calculation approaches. This similarity is due to the fact that the asymptotic behavior in χ' and χ'' against the reduced field ($h,\eta \ll 1$ or $h,\eta \gg 1$) for both models is almost the same, compare Eq. (2.13) with Eq. (2.22). The same asymptotic behavior of M as a function of the reduced field is also found for the two models, compare Eq. (2.10) with Eq. (2.19). If we assume a constant temperature, Fig. 2.3 then represents profiles of χ' and χ'' versus the applied field amplitude H_0. On the other hand, the profiles of χ' and χ'' versus

temperature, for a fixed applied field amplitude, are quite different from those in Fig. 2.3. The temperature dependent χ' and χ'' will be shown in Section 2.6.

It is interesting to note that the interpretation of j_c values in the above two models can differ by a factor of two, see Eqs. (2.14) and (2.23). In other words, the simplified model gives larger critical current than that obtained for the realistic model. That could be expected because the simple model does not include the shielding currents in the vortex-free region. The critical current j_c should be evaluated by using the realistic formula (2.23).

The above model calculations show that when the external field is small enough, a superconducting thin film has perfect diamagnetic response demonstrated by the perfect diamagnetic susceptibility χ_0 (simplified) or χ_{00} (realistic). It is interesting to note that χ_0 is about twice as large as χ_{00}. This difference is due to the fact that the simplified model requires the screening currents twice as large as those of the realistic model. This is a consequence of the fact that the currents in the simplified model are distributed in the outer peripheral region, whereas the currents in the realistic model are distributed over the entire film, see Chapter 3.

The realistic model predicts a deeper flux penetration depth (0.7R) at the χ''_{max}, compared to that for the simplified model (0.6R). Investigation of flux penetration by the scanning Hall probe technique (see Chapter 3) showed that the realistic penetration depth is much closer to the experimental observations.

2.3. Sample preparation and characterization

The HTS thin-film samples were prepared by CTF Systems Inc. The YBCO films were deposited on heated $LaAlO_3$ substrates by pulsed laser ablation. A Lambda Physik LPX2051 KrF excimer laser (λ = 248 nm) equipped with special

electrodes to improve the beam profile uniformity was used. The pulses, with a repetition rate of 5–10 Hz and a fluence of 1.5 J/cm^2, were focused to an area of 4 × 2 mm^2. An oxygen pressure of 200 mTorr (≈ 27 Pa) and a substrate heater temperature of 820 °C were maintained during the film deposition. The target holder was a Kurt J. Lesker Co. PolyGun system which holds six high density sintered YBCO targets in a hexagonal carousel rotated under computer control. After deposition, the films were cooled slowly (5 °C/min) in 600 Torr (≈ 8 × 10^4 Pa) of oxygen. The resulting film thickness ranged from 300 to 400 nm. The films were very smooth, exhibiting a mirror-like appearance.

Prior to the ac susceptibility measurements, the structural qualities of the films were investigated using X-ray diffractometry, Raman spectroscopy and Auger spectroscopy [Chrzanowski et al. 1991; Xing et al. 1993]. Those studies showed that the YBCO thin-film samples used for the ac susceptibility measurements were highly c-axis oriented, fully oxygenated, and they were homogenous over the film thickness, see Fig. 2.4. Microscopic observations by scanning electron microscopy (SEM) revealed no voids or cracks. Table 1 shows the sample characteristics and their j_c values at 77 K.

Table 1. Characteristics of the Y-Ba-Cu-O thin films.

Sample	Thickness (nm)	Size (cm)	T_c (K)	j_c (77 K) (A/cm^2)
Y29	400	1 cm × 1 cm	89.5	6.0×10^5
Y31	400	1 cm × 1 cm	89.9	2.4×10^6
Y58	300	1.4 cm × 1.2 cm	91.7	3.7×10^6
Y259	300	1.1 cm × 1.1 cm	89.7	3.0×10^6

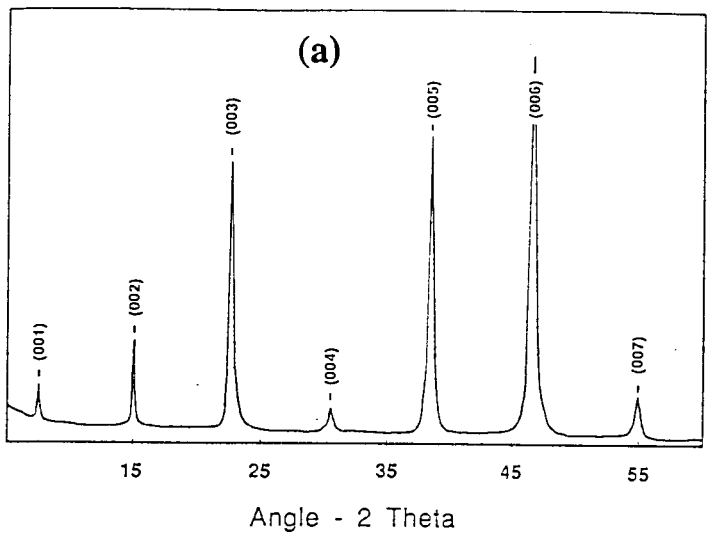

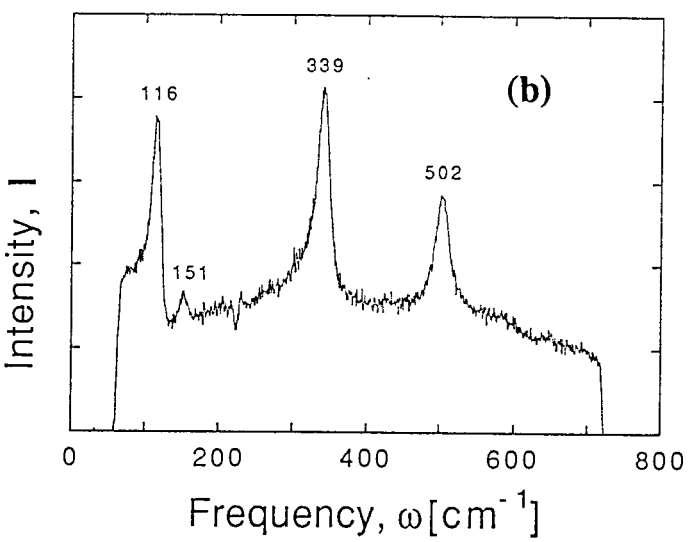

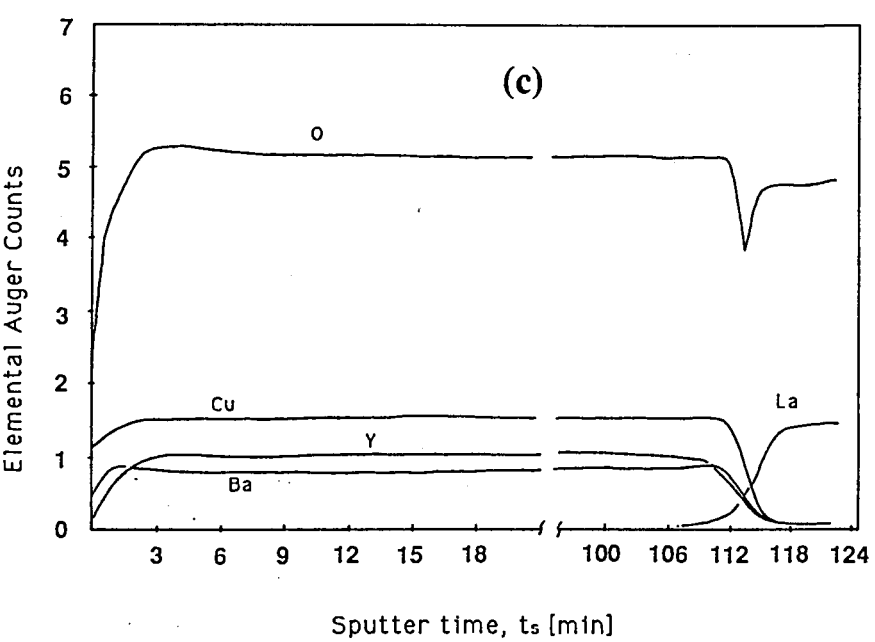

Fig. 2.4. (a) X-ray diffraction pattern of a YBCO thin film deposited by laser ablation on $LaAlO_3$ single crystal. Strong (00ℓ) Bragg reflections indicate a highly c-axis oriented texture. (b) Unpolarized Raman spectrum of a YBCO thin film indicating c-axis orientation of the film. The spectral position (502 cm^{-1}) of the bridging oxygen, O(4), peak indicates full oxygenation. (c) AES elemental depth profile of a YBCO thin film. Except for narrow interfacial regions, excellent film uniformity can be seen.

2.4. Experimental setup

Figure 2.5(a) shows the coil arrangement of the ac susceptometer we built for this study of thin-film samples. The pick-up coil and the compensation coil were balanced and coaxially mounted inside a driving coil. The thin-film sample was placed in the center of the pick-up coil with its plane perpendicular to the coil axis. The diameters of the coils were large compared with the size of the film so that the signal from the film can be approximated by a magnetic dipole moment. A sapphire tube was used as the coil form which helps to achieve an isothermal environment. A smaller sapphire tube supporting the film provided adequate thermal connection between the sample and a thermometer. The sample-coil assembly was cooled by a cold finger and exchange gas. The film temperature was controlled by a resistor heater located away from the coils. All metal structural components were well separated from the coils to avoid eddy-current signals.

A high-permeability cylinder surrounding the Dewar reduced the Earth's magnetic field to ~ 10^{-7} T (measured by a Bell model 620 gaussmeter). The ac driving current was provided by a power amplifier driven by the oscillation output of the lock-in amplifier (usually at 1 kHz) with a 1 kΩ external resistor in series with the driving coil (its resistance was about 3 Ω at 77 K), see Fig. 2.5(c). Alternatively, a home-made voltage-current converter was used for this purpose. The sample temperature was swept at a rate < 0.3 K/min with a temperature controller (LakeShore DRC-91CA). The data were recorded in temperature intervals of < 0.1 K. A lock-in amplifier (Princeton Applied Research 5209) was used to detect the pick-up coil voltage at the fundamental frequency. Both in-phase and out-of-phase pickup voltages were recorded. In order to separate the real and imaginary components of the ac susceptibility, the phase angle of the lock-in amplifier was first adjusted to null the out-of-phase signal when the film

was in the diamagnetic shielding or low-loss state. After data acquisition, a fine phase adjustment was made mathematically [Goldfarb et at. 1992] to bring the normal- and low-temperature χ'' values to zero.

There was a small offset pickup voltage due to the mismatch between the pick-up and compensation coils. But this was readily subtracted from the total signals. Most of the data were collected for the zero-field-cooled (ZFC) process, although we found that, for our maximum field of about 3 mT rms, the difference between ZFC and FC (field-cooled) curves was small.

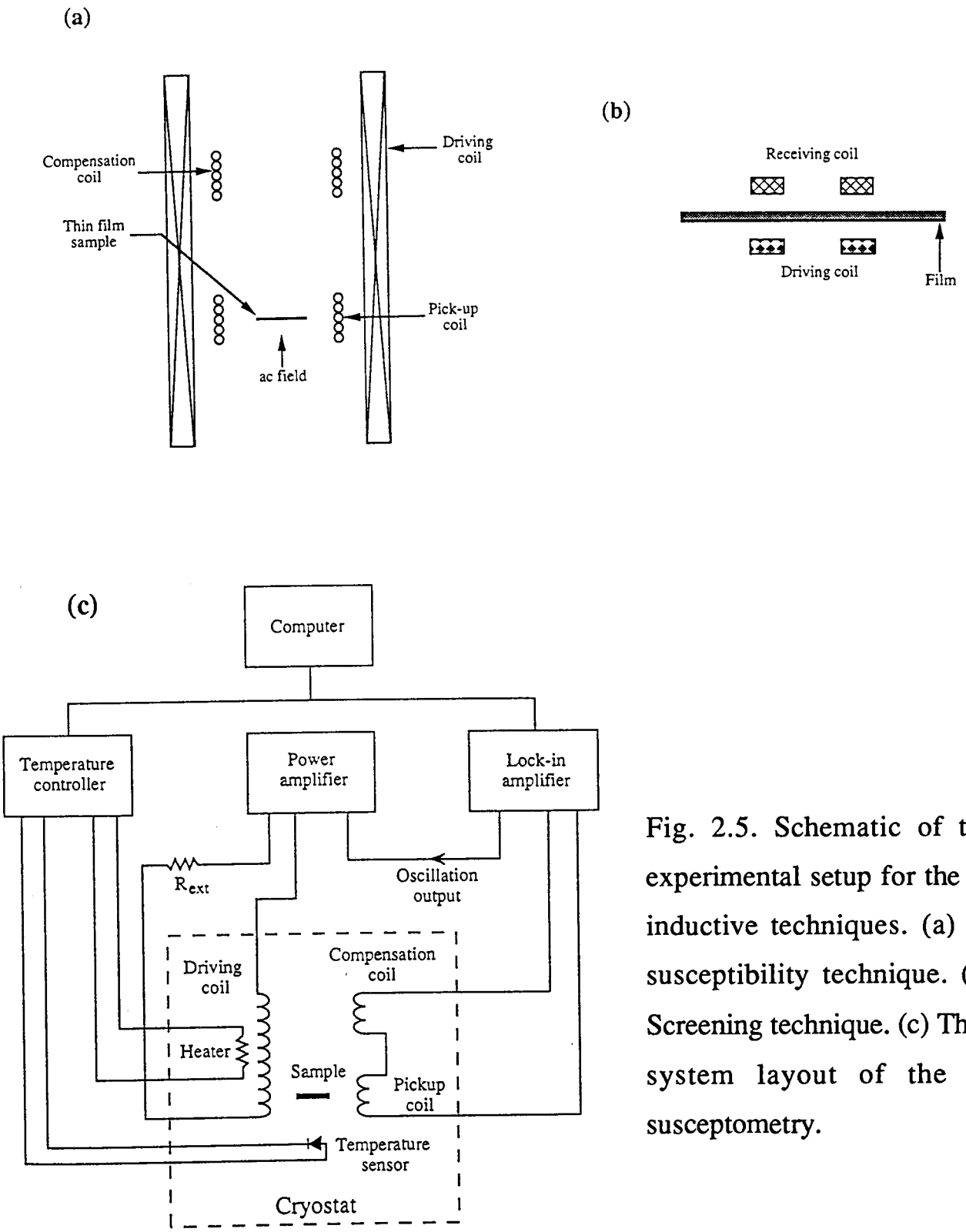

Fig. 2.5. Schematic of the experimental setup for the ac inductive techniques. (a) ac susceptibility technique. (b) Screening technique. (c) The system layout of the ac susceptometry.

2.5. AC screening method

In parallel with the susceptibility method, the ac screening technique [Claassen et al. 1989, 1991, 1992] was also used to determine the critical current densities for the same films. The apparatus consisted of a pair of small pancake-shaped coils pressed against each side of the film substrate, as shown in Fig. 2.5(b). The mean diameters of the coils (~ 5 mm) were about half of the size of the film. A thin Kapton film placed in front of each coil formed a smooth coil-sample interface, and ensured a distance from the top of the driving coil to the film surface of < 1 mm. A 1 kHz ac driving current induced the current in the superconducting film, and the signal due to the leaking of the flux lines through the film was picked up by the receiving coil. The induced sheet current density J can be calculated by curl **B** from this configuration when $J < J_c$. The screening effect is sufficiently strong so that at the surface of the film the normal component of the magnetic field vanishes. Once the coil-film distance is fixed, J is proportional to the driving current. During the measurement, the coil-film assembly was cooled by nitrogen vapor or directly immersed into liquid nitrogen, and the driving current was increased from zero at constant temperature. A small signal proportional to the driving current can be detected initially, due to the flux leakage around the edge of the film. When J_c was exceeded, there was a sudden increase of the signal amplitude together with a strong signal distortion caused by the flux penetration through the film.

One should be aware of the differences between these two ac methods. The screening method is sensitive to a local area, which is adjacent to the driving coil, and this is the place where the flux first penetrates through, whereas the ac susceptibility method measures the whole sample and therefore provides a gauge of the average quality. Agreement of the J_c values obtained from these two methods, therefore, should suggest uniform critical current density over the film.

2.6. Results and discussion

Figure 2.6 shows the temperature dependence of ac susceptibility for a typical YBCO thin-film sample (Y259). The same measurement scheme was applied to the other YBCO and to TBCCO thin films and the results were shown in Xing et al. 1993. The family of curves in Fig. 2.6 corresponds to different ac field amplitudes, $\mu_0 H_a$ = 0.001, 0.1, 1, 10, 20, and 30 × 10^{-4} T (rms), for f = 1 kHz.

We have shown in Section 2.2.3 that the theoretical ac susceptibility is a function of the reduced field $\eta \propto H_0/j_c(T)$. For fixed applied field amplitude H_0, χ becomes a function of temperature via $j_c(T)$. Using a measured $j_c(T)$ (see discussion below) and Eq. (2.20) (the realistic model), we calculated the temperature-dependent susceptibilities of the YBCO film, shown in Fig. 2.6 in dashed lines. The susceptibilities presented here are proportional to the external susceptibilities. The onset of the low field (e.g. $\mu_0 H_a = 10^{-7}$ T) measurement determines the superconducting transition temperature, $T_c \sim 90$ K, with a transition width $\Delta T \sim 0.5$ K. The $\chi''(T)$ shows a maximum. Further below T_c, both the $\chi'(T)$ and $\chi''(T)$ curves become flat, demonstrating the complete diamagnetic shielding and the low-loss state, respectively.

For applied flux density $B_a \leq 10^{-4}$ T, the measured χ' shows a tail after the initial sharp transition, and the χ'' peak width is wider compared to that obtained from the calculations. This behavior was caused by defects, which were not detectable by optical and SEM observations, that allowed additional flux penetration into these regions. The presence of defects was independently shown by scanning Hall probe maps (see Chapter 3). The measured values of $\chi''(T)$ peak heights are lower than those obtained from the calculations due to the presence of defects and due to a strong dependence of j_c on the applied ac field amplitude near T_c [Xing et al. 1994a].

The position of the χ'' peak, T_p, shifts to lower temperatures with an increasing driving field H_a. This is to be expected because when the driving field amplitude increases, larger screening currents are needed to maintain the critical state in which the applied flux nearly fully penetrates the sample. This is achieved by lowering the sample temperature.

The influence of defects is most evident near T_c, as is demonstrated by the transition step in $\chi'(T)$ and by the accompanying shoulder in $\chi''(T)$ for $\mu_0 H_a = 10^{-5}$ T. The signature for sample inhomogeneities disappears in the ac susceptibility curves of $\chi'(T)$ and $\chi''(T)$ for large driving fields, $\mu_0 H_a \geq 1$ mT. Similar behavior was observed for other YBCO thin film samples, see [Xing et al. 1993]. At higher ac fields or lower temperatures the calculations and measurements are in good agreement.

Figure 2.7 shows both the measured and the calculated ac susceptibilities as a function of the applied ac field at a driving frequency f = 1 kHz. The $\chi''(H_a)$ peaks appear at $\mu_0 H_a \approx 16$ and 79×10^{-4} T (rms) for T = 85 and 77 K, respectively. The discrepancy between the calculated and the measured $\chi(H_a)$ curves at T = 77 K is due to the fact that the 77 K data cover a large field range and therefore the field dependence of j_c is more pronounced. The scanning Hall probe [Xing et al. 1994a] measurements using the applied field $\mu_0 H_a \approx 110 \times 10^{-4}$ T (which corresponds to the amplitude of the ac field at which a maximum in $\chi''(H_a)$ occurred when the sample was maintained at 77 K, see Fig. 2.7) showed that the flux penetration reached the center of the sample. The calculations predict a smaller penetration depth, $L^* \approx 0.7R$. This discrepancy is caused by the field dependent critical current in the measured films.

Using Eq. (2.23) we determined the values of the critical current density as a function of temperature. The peak temperatures T_p and fields H_p were identified from the $\chi''(T)$ and $\chi''(H_a)$ curves, respectively. The uncertainties of T_p and H_p

are less than 0.1 K and 0.5×10^{-4} T, respectively. Figure 2.8 shows the critical current density j_c as a function of temperature from the above measurements. The temperature range over which the $j_c(T)$ was determined was limited by the highest ac field amplitude available. For good quality superconducting films, a large applied field is needed to drive the $\chi''(T)$ peak to lower temperatures.

The j_c values for $T_c - 15 < T < T_c$ can be fitted with a simple power law $j_c(T) = j_{c0}(1 - T/T_c)^n$, where the value of the exponent n is ≈ 1.64. Similar power laws for the temperature-dependent j_c were observed for other YBCO thin films [Xing et al. 1993]. The j_c values were compared with other measurements. For example, at 77 K, the j_c values were about 3.0, 4.4, and 2.5×10^6 A/cm^2 (average value) for the ac susceptibility, ac screening [Xing et al. 1993], and scanning micro-Hall probe [Xing et al. 1994a] measurements, respectively. A fair agreement among different measurements on the same film validates the model calculation used in the data analysis. It also indicates that the sample is fairly homogenous over a large area. The detailed measurements of the flux distribution above the sample, see Chapter 3, by a flux mapping technique support strongly the above conclusions.

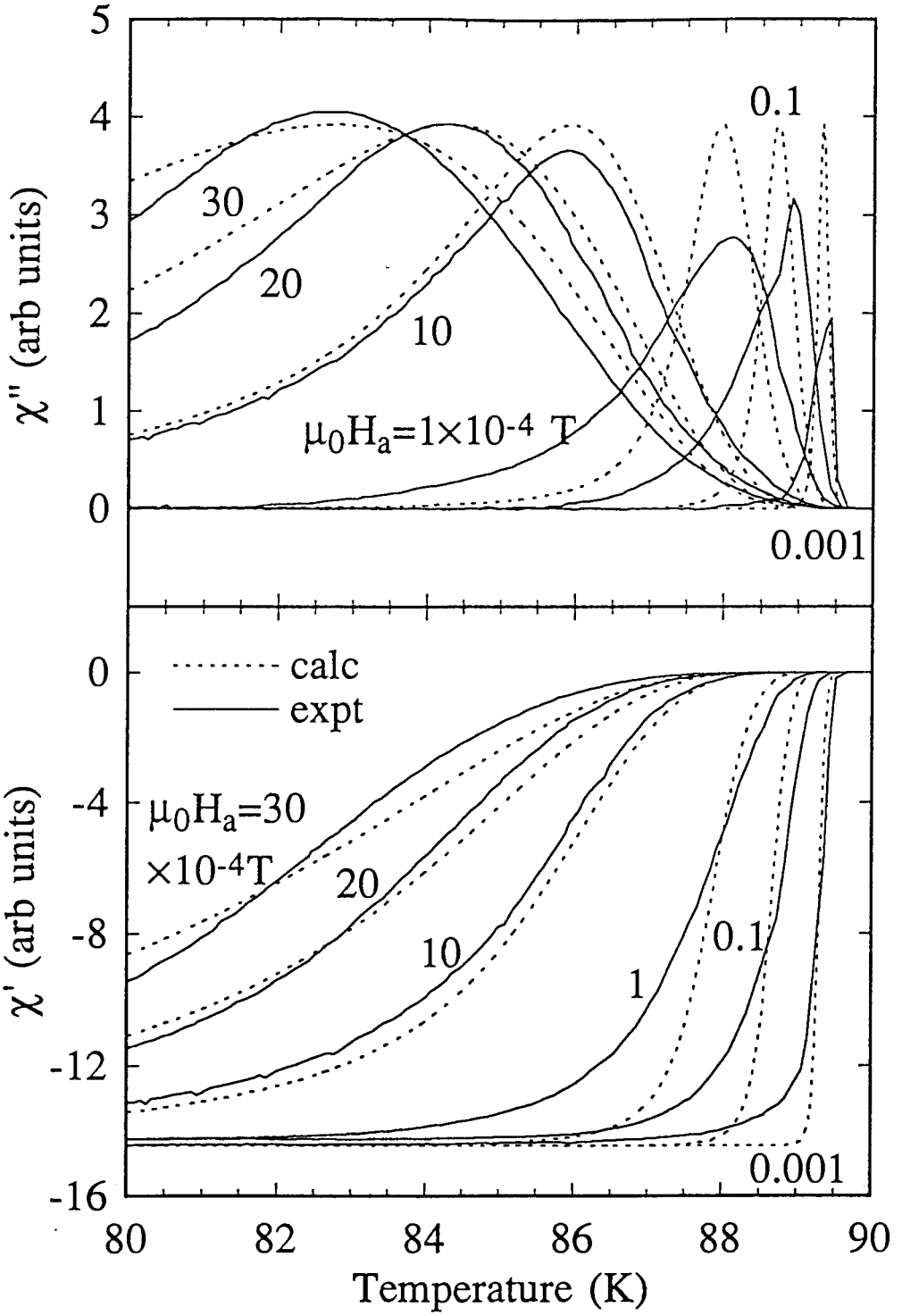

Fig. 2.6. Measured (solid lines) and calculated (dashed lines) ac susceptibilities of a YBCO thin-film sample (Y259) as functions of temperature for six different ac field amplitudes, $\mu_0 H_a$ = 0.001, 0.1, 1, 10, 20, and 30 × 10^{-4} T (rms). The driving frequency f = 1 kHz.

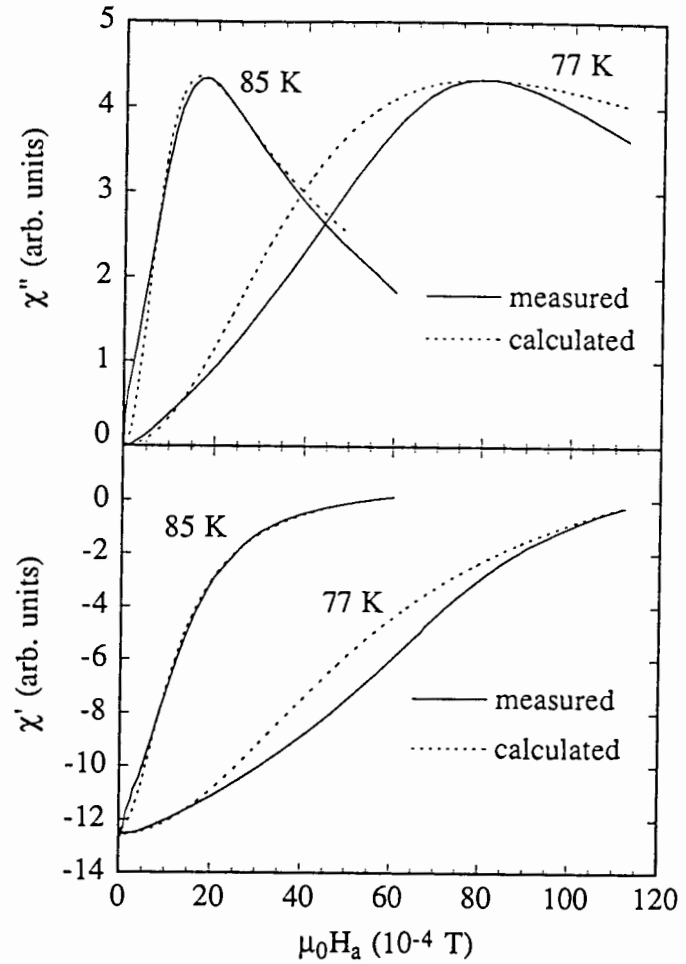

Fig. 2.7. Measured (solid lines) and calculated (dashed lines) ac susceptibilities as functions of the applied ac field. The driving frequency f = 1 kHz.

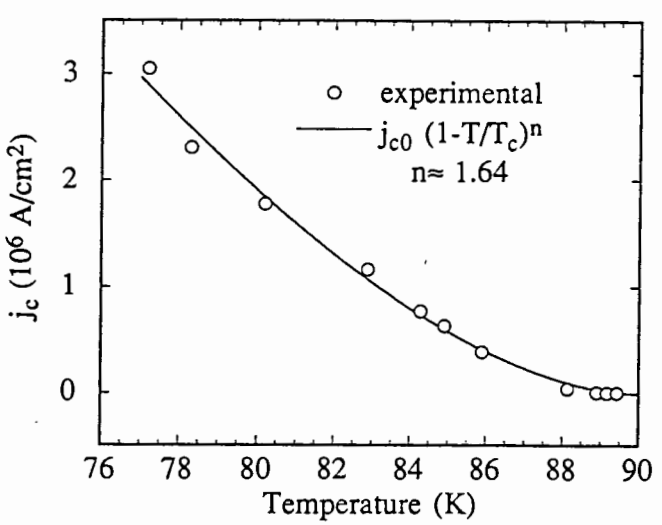

Fig. 2.8. The critical current density j_c as a function of temperature determined from the ac susceptibility measurement.

2.7. Frequency dependence

Based on the Anderson-Kim flux creep theory [Anderson 1962; Anderson and Kim 1964], the critical current density j_c of a superconductor is given by [Campbell and Evetts 1972; Malozemoff et al. 1988],

$$j_c = j_{c0}\left[1 - \frac{kT}{U}\ln(f_0 / f)\right], \tag{2.24}$$

where j_{c0} is the critical current density in the absence of thermal activation (T = 0), k is the Boltzmann's constant, U is the flux pinning potential which is dependent on the temperature and field, f_0 is the characteristic frequency [Blatter et al. 1993], and f is the driving frequency of an applied ac field. Equation (2.24) shows that the apparent value of j_c increases with an increasing driving frequency, and decreases with an increasing temperature.

The activation barrier U is given by $U = \frac{1}{2} p\mu_0 H_c^2 V_c$, where H_c is the thermodynamic critical field, $\frac{1}{2}\mu_0 H_c^2$ is the condensation energy, V_c is the activation volume, and p is a material constant which depends on the nature of material imperfections. The activation volume $V_c \approx a_0^2 L_c$ [Malozemoff et al. 1988; Kes et al. 1989], where $a_0 = 1.075\sqrt{\Phi_0 / B}$ is the flux line spacing, L_c is the correlation length along the flux line which is approximately equal to the coherence length ξ, and B is the internal flux density. According to the Ginzburg-Landau theory, near T_c and for a large Ginzburg-Landau parameter κ, $H_c \sim (1 - t)$, and $\xi \sim (1 - t)^{-1/2}$, where $t = T/T_c$ is the reduced temperature. It follows that $U \sim (1 - t)^{3/2}/B$. In ac susceptibility measurements which are carried out in the absence of dc applied field, the internal B field will be replaced by the amplitude of the ac driving field H_a.

The maximum in $\chi''(T)$ is reached when the value of the critical current satisfies Eq. (2.23). Recall that the temperature at which $\chi''(T)$ reaches its peak value is denoted as T_p. When the driving frequency f increases, the critical current density j_c also increases, see Eq. (2.24); therefore, the sample temperature has to be increased in order to satisfy Eq. (2.23). One expects that j_c in Eq. (2.24) remains approximately unchanged over the range of applied ac frequencies f,

$$j_c = j_{c0}\left[1 - \frac{kT_p}{U}\ \ln(f_0 / f)\right] \approx \text{constant.} \qquad (2.25)$$

Using $U \sim (1 - t_p)^{3/2}/H_a$ leads to

$$(1 - t_p)^{3/2}\ t_p^{-1} \approx (H_a / H_e)\ \ln(f_0 / f), \qquad (2.26)$$

where $t_p = T_p/T_c$, and H_e and f_0 are constants to be determined experimentally.

Our frequency-dependent ac susceptibilities were measured in the absence of dc fields. For a fixed ac field amplitude [$\mu_0 H_0 /\sqrt{2} = \mu_0 H_a = 10^{-4}$ T (rms)], Fig. 2.9 shows the plot of T_p as a function of f. The frequency range was from 10 to 10^5 Hz. The H_a–T_p dependence shown in Fig. 2.10 (for a fixed driving frequency f = 1 kHz) follows a power law $H_a \sim (1 - t_p)^n\ t_p^{-1}$ with $n \approx 1.54$, $\mu_0 H_e \approx 1$ T, and $f_0 \approx 2 \times 10^{12}$ Hz. The value of n is very close to exponent 3/2 in Eq. (2.26).

Equation (2.24) can be used to estimate the pinning potential. $j_c(T = 0) = j_{c0}$ was estimated by using extrapolation from Fig. 2.8. At T = 77 K and for f=1 kHz and $B_a = 10^{-4}$ T, Eq. (2.24) leads to the pinning potential $U \approx 0.16$ eV. This value is consistent with that obtained from a flux noise measurement [Ferrari et al. 1990].

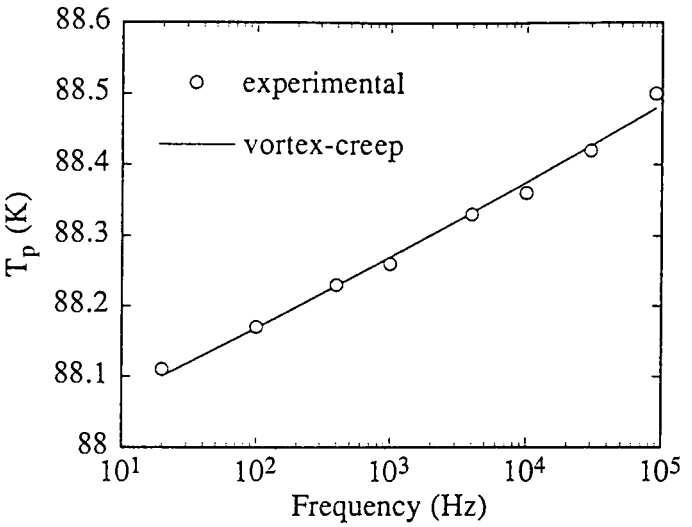

Fig. 2.9. T_p versus f with $\mu_0 H_a = 10^{-4}$ T (rms). The line is a fit with Eq. (2.26).

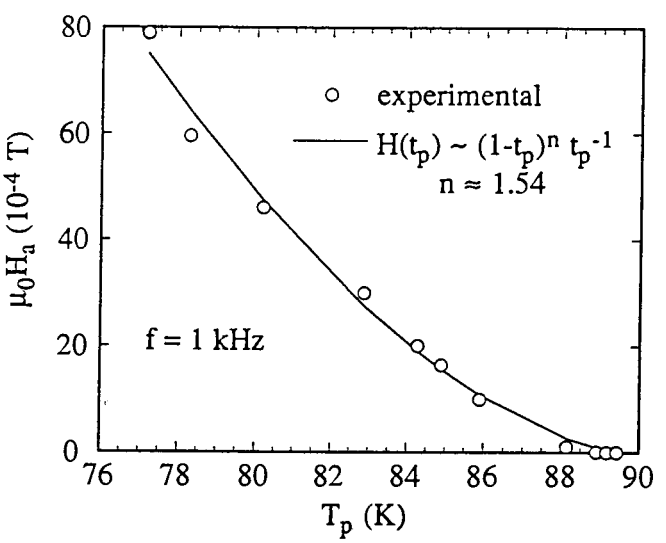

Fig. 2.10. H_a versus T_p for f = 1 kHz.

2.8. Conclusions

The fundamental frequency ac susceptibilities of several $YBa_2Cu_3O_{7-\delta}$ thin films were measured as functions of temperature and the applied field, with film surface oriented perpendicular to the applied field. Also inductive screening measurements were carried out for determining the j_c of the same films. The theoretical ac susceptibilities, calculated from the realistic current distributions in thin film geometry [Mikheenko and Kuzovlev 1993; Zhu et al. 1993; Clem and Sanchez 1994a], agree well with the overall experimental data over a wide range of temperature and applied field. The constant maximum value in the calculated $\chi''(T)$ curves is satisfied at high fields and at low temperatures.

The ac susceptibility technique is a sensitive diagnostic tool for the detection of superconducting defects in the superconducting thin films. The presence of sample inhomogeneities is particularly visible in the measurements of χ', χ'' at small driving field amplitudes. For large driving fields, the transition width, measured by $\chi'(T)$, is broadened and the peak width of $\chi''(T)$ is noticeably increased, see Fig. 2.6.

The temperature-dependent critical current density determined by ac susceptibility measurement is in good agreement with the current densities determined by ac screening [Xing et al. 1993] and scanning Hall probe [Xing et al. 1994a] measurements. A simple power law for $j_c(T)$ was observed, $j_c(T) = j_{c0}(1 - T/T_c)^n$, with $n \approx 2 \pm 0.5$ for all measured samples [Xing et al. 1993].

The observed frequency-dependence of the χ'' peak temperature T_p can be explained well by scaling argument [Malozemoff et al. 1988] based on flux creep theory [Anderson 1962; Anderson and Kim 1964]. In this model the apparent critical current increases with an increasing driving frequency f and that results in a reduction of the depth of flux penetration. The sample temperature has to be increased in order to recover the full flux penetration which is required to reach

the maximum value of $\chi''(T_p)$. The above results show that thermal activation plays an important role in vortex motion in HTS films. The activation barrier U was found to be ≈ 0.16 eV, at T = 77 K and for the applied flux density $B_a \sim 10^{-4}$ T.

The present work demonstrates that the ac susceptibility technique is a simple and effective means for characterizing high-T_c superconducting thin films. The measurements carried out by varying different parameters, i.e. temperature, the applied field, and driving frequency, enable one to obtain valuable insight about the flux dynamics in the high-T_c superconducting thin films.

Chapter 3
Magnetic Flux Mapping and Current Distributions

Magnetic flux mapping or imaging of a superconductor can be carried out with a scanning Hall probe and a magneto-optical technique. We concentrate in this chapter on the use of a scanning micro-Hall probe for flux mapping of HTS thin films. Calculation procedures converting the flux maps into current distributions are discussed.

3.1. Introduction

Two types of Hall probe systems, distinguished by stationary or scanning operation, have been employed for magnetic flux mapping of HTS thin films. The magnetic flux density B_z normal to the film surface is usually measured. Scharen et al. [1991] used a stationary Hall probe with an active area about 1 mm^2 for the measurements of local fields above a HTS thin-film sample. This was a one point measurement (maximum remanent field) which allowed them to determine only the average critical current density. Rauch et al. [1992] developed a scanning Hall probe system that has an active area about 0.5 mm^2. The averaged critical current density was also estimated from the remanent field measurement.

Scanning Hall probes are capable of measuring the magnetic flux profiles across the whole sample. Brüll et al. [1991] used a scanning Hall probe with an active area about 0.04 mm^2 to measure the flux distribution above their HTS thin-film samples. These results were used to complement the flux images obtained by a magneto-optical method; however no inverse calculations were carried out.

Roth et al. [1989] pointed out that when the current distribution is two-dimensional (2D), the solution of the inverse problem (from the field map to the

current distribution) is theoretically possible and the interpretation is, in principle, unique. They proposed an algorithm using a technique based on Fourier analysis. Keith and Smith [1993] used this algorithm to calculate the current distribution from their scanning Hall probe measurements on polycrystalline disks (12 mm in diameter and 3 mm thick). Asher et al. [1982] proposed a loop current method in which the current can be deduced from a matrix equation using the magnetic flux distribution. We have used this method for the interpretation of scanning Hall probe measurements and magneto-optical images which were obtained on some of our $YBa_2Cu_3O_{7-\delta}$ (YBCO) and Tl-Ba-Ca-Cu-O (TBCCO) thin films [Grant et al. 1994].

In this chapter, we present detailed studies of the magnetic field penetration of square-shaped epitaxial YBCO thin films. These studies were carried out using a scanning micro-Hall probe with an active area of ~ 25 × 25 μm. The flux mapping was performed either in the presence of an applied field or in the remanent state, and the flux penetration was studied as a function of the applied field magnitude. The film thickness, d ~ 300 nm, is comparable to the London penetration depth. The measured field above the film was interpreted assuming that the induced supercurrents can be well described by a 2D current distribution, neglecting the variations of the current across the film thickness. Calculation procedures were developed to construct the sheet magnetization M(x,y) and the 2D current distribution in the film from the measured flux density above the sample surface. Here the sheet magnetization M is normal to the film plane (parallel to z-axis). The current distribution was measured as a function of the applied field. It will be shown that the measured hysteresis magnetization loops can be constructed using a generalized superposition principle [Brandt et al. 1993]. This procedure allows one to gain a better insight into the hysteresis behavior of square-shaped superconducting samples.

This chapter is organized as follows: Section 3.2 describes experimental details, Section 3.3 discusses the inverse calculations, Section 3.4 presents the experimental measurements and the result of calculations, and Section 3.5 illustrates the validity of the superposition principle.

3.2. Experimental details

3.2.1. Measuring system

Figure 3.1 is a schematic diagram of the scanning micro-Hall probe system, which is a customized commercial device developed by Quantum Technology Corp. [Quantum] in collaboration with our high-T_c group at Simon Fraser University. We have been actively involved in the design, assembly, and test of the system. A closed-cycle refrigerator (CTI model 22) was used to provide the cooling power. The thin-film sample was mounted to the cold head which then cools the sample to a minimum temperature of 10 K. A heater connected to a temperature controller (LakeShore DRC-91 CA) was used to control the sample temperature. An aluminum cylinder thermally attached to a 70-K stage was used to provide the thermal shield for the sample space. The heat exchange between the Hall probe and the shielding cylinder was achieved through a braided copper wire. The Hall probe temperature was normally stabilized around 85 K during the measurement and was independent of the sample temperature.

The Hall probe with an active area of 25 × 25 μm was patterned from a GaAs quantum-well heterostructure thin film (University of Bath). A constant dc current of 0.1 mA was applied to the current leads of the sensor. A nanovoltmeter (Keithley 182) was used to detect the Hall voltage, which is proportional to the axial (z) component of the magnetic flux density, B_z. A pair of Helmholtz coils with a diameter of 10 cm provided an axial magnetic field H_a

perpendicular to the surface of the film. The typical size of the sample is ~1 cm, and therefore the axial external field was considered to be uniform across the sample area. The calibration of this external field was carried out by a Bell 620 gaussmeter. The scanning micro-Hall probe has a sensitivity of about 0.17 V/T at 85 K, and with a typical noise voltage of ~ 3 μV, this corresponds to a field sensitivity of ~ 2×10^{-5} T. The Hall sensor was mounted to a stainless steel tube which was scanned with an X–Y position stage. The lateral movement was controlled by two precision stepping motors with scan resolution of about 2.5 μm, and the whole system was controlled by a computer when undertaking the raster scan.

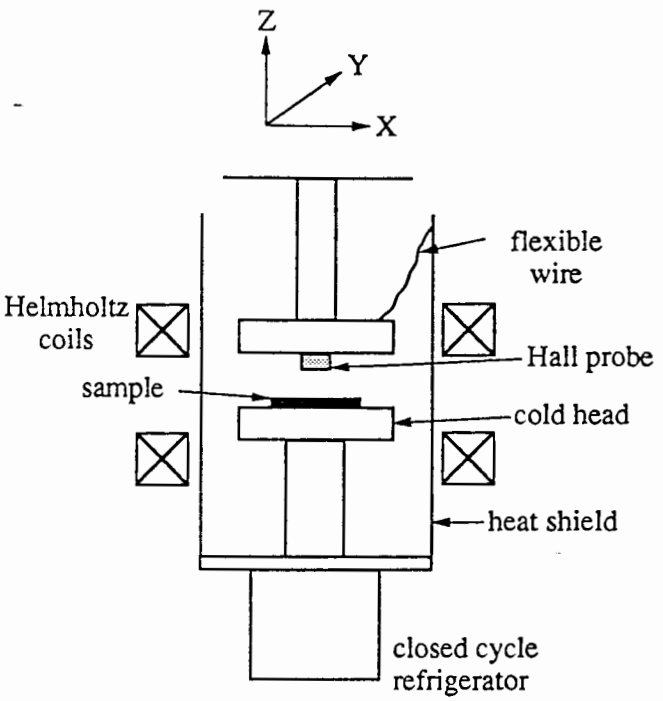

Fig. 3.1. Schematic diagram of the scanning micro-Hall probe system.

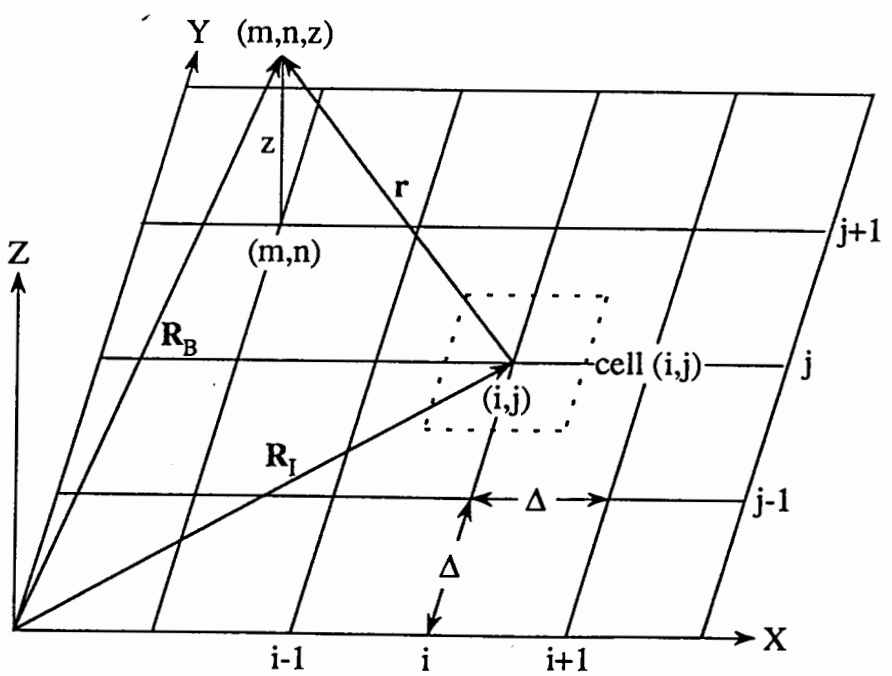

Fig. 3.2. Grid representation of the Hall probe raster scan.

3.2.2. Measuring procedure

In a typical measurement, the Hall sensor was adjusted to a height z ~ 250 μm above the sample surface. This distance was chosen to protect the delicate Hall probe from accidental damage which could occur during wide lateral sweeps. The raster scan was carried out either in the presence of an applied field (field-on) or with the applied field decreased to zero (remanence). In both cases, the sample had always been zero-field-cooled from room temperature to a desired temperature before an external field was applied to the sample. The measurements were carried out mostly at liquid N_2 temperatures. The magnitude of the applied flux density $\mu_0 H_a$ was varied systematically in the range from 0 to 30 mT and the raster scan was repeated for each applied field. The lateral step size was set to 0.3 mm leading to 41 × 41 grid points for a single lateral scan. Each data point requires one second acquisition time. It took ~ 30 minutes to complete the measurement. The Hall probe signal of the remanent field was found to decay logarithmically with time. The time dependence of the magnetic flux can be estimated by monitoring the time dependence of the B field at one point (usually around the center). It was found that the strength of the remanent flux density decreased by a small amount (a few percent) over the period of the measurement and therefore the role of flux creep was neglected in the interpretation of data.

3.2.3. Thin-film samples

The growth conditions for the preparation of high quality epitaxial YBCO thin films were described in Chapter 2. The Hall probe studies were carried out on a number of samples, see for example [Grant et al. 1994]. In this chapter data are presented for the film (sample Y259) which exhibited the best lateral

homogeneity among available samples. The critical temperature of the film was 89.7 K, as determined by ac susceptibility measurements. The film lateral dimensions were ~1.08 × 1.08 cm^2, and the thickness d ≈ 300 nm.

3.3. Inverse calculation

In this section we present the method for generating the sheet current distribution from the Hall probe maps. We demonstrate that our calculation procedure provides very reliable results.

3.3.1. Linear equations

The change of an applied field induces electric currents in a thin-film superconductor. Since the thickness of the HTS thin film, d, is comparable to 2λ, where λ is the London penetration depth, the supercurrent is considered uniform over the thickness and therefore can be described by a sheet current density J (in units of A/m). The volume current density is given by j = J/d (in units of A/m^2). Since there is neither a current source nor a sink in the film, the induced supercurrents must circulate in closed loops; that is, for the static case, continuity of flow has to be satisfied, $\nabla \cdot \mathbf{J} = 0$. The equation of continuity is satisfied automatically by using the concept of sheet magnetization **M** (magnetic moment per unit area, in units of amperes). The sheet current density is $\mathbf{J} = \nabla \times \mathbf{M}$. The usual volume magnetization is given by M_{vol} = M/d (in units of A/m). Since the sheet current is confined to the sample surface (x–y plane), the only non-vanishing magnetization component is along the z-axis. We can write

$$\mathbf{J} = \left(J_x, J_y\right) = \left(\frac{\partial M}{\partial y}, -\frac{\partial M}{\partial x}\right) \tag{3.1}$$

Using Ampere's law and $\mathbf{J} = \nabla \times \mathbf{M}$ leads to

$$\nabla \times \mathbf{H} = 0, \tag{3.2}$$

where $\mathbf{H}$ is the magnetic (internal) field and the induction $\mathbf{B} = \mu_0(\mathbf{H} + \mathbf{M}_{vol})$. Equation (3.2) is the equation of magnetostatics without free currents. Therefore the field $\mathbf{H}$ is a sum of the external field, $\mathbf{H}_a$, and the demagnetizing field $\mathbf{H}_d$ caused by the static magnetization $\mathbf{M}_{vol}$.

The Hall probe raster scan is schematically represented by the x-y grid in Fig. 3.2. The measured field points are represented by a point (m,n,z). Here the integer indices (m,n) represent the spatial coordinates ($x_m = m\Delta$, $y_n = n\Delta$, see Fig. 3.2) of the measured field. Note that for a particular raster scan, z is a constant. It is important to point out that one measures the z component of the local magnetic flux density, which includes the applied flux density ($\mu_0 H_a$) and the flux density (self-induction) $\mu_0 H_S$ from the supercurrents in the film. The self-induction can be extracted by subtracting the applied flux density from the measured flux density.

The distribution of the magnetization M on a finite grid (with the grid coordinates (i,j), see Fig. 3.2) can be represented by the average values M(i,j) over the grid cell (i,j) (the square area centered at (i,j) as indicated by the dashed lines). The magnetic induction $B_{0z}(m,n,z)$ from the magnetic moment in cell (i,j) can be written as [Jackson 1975],

$$\begin{aligned} B_{0z}(m,n,i,j,z) &= \frac{\mu_0}{4\pi} M(i,j) \int_{S'_{i,j}} \frac{3z^2 - r^2}{r^5} dx'\, dy' \\ &= M(i,j) G(m,n,i,j,z), \end{aligned} \tag{3.3}$$

where r is the distance between the source point (i,j) and the field point (m,n,z). The integral G(m,n,i,j,z) in Eq. 3.3 is calculated over the area of the cell (i,j). G(m,n,i,j,z) is a function of geometrical variables only. The total magnetic induction $B_z(m,n,z)$ (flux density) is given by adding all contributions,

$$B_z(m,n,z) = \sum_{i=1}^{N1} \sum_{j=1}^{N2} M(i,j) G(m,n,i,j,z), \tag{3.4}$$

where N1 and N2 are the total number of data points (or scanning steps) in the x and y directions respectively. For a raster scan that has an equal number of scanning steps in both directions, N1 = N2 = N and the total number of data points is N^2. In a typical measurement the raster scan is extended to outside of the film area to obtain complete information.

Equation (3.4) is a set of linear equations for M(i,j). We have a system of N^2 linear equations for N^2 unknowns M(i,j) that can be represented by the following matrix equation,

$$\mathbf{G} \cdot \mathbf{M} = \mathbf{B_z}, \tag{3.5}$$

where **G** is a matrix of order $N^2 \times N^2$, and **M** and $\mathbf{B_z}$ are both column vectors of dimension N^2 in matrix notation. The magnetization vector M(i,j) in Eq. (3.5) was determined by two methods: direct solution of the matrix equation and an iteration procedure.

3.3.2. Matrix inversion

The direct solution is given by

$$\mathbf{M} = \mathbf{G}^{-1} \cdot \mathbf{B}_z. \qquad (3.6)$$

The inverse matrix $\mathbf{G}^{-1}$ was calculated by a method of LU decomposition using forward and backward substitution, where L and U stand for lower and upper triangular matrices respectively, see Press et al. 1985. Typically, the raster scan has $N^2 = 1681$ data points ($N = 41$), resulting in $N^4 \sim 3$ million total matrix elements in G. This takes about 12 MBytes (MB) of computer memory in floating point format to calculate the inverse matrix G^{-1}. An IBM compatible, 486/66 DX2 personal computer (PC) with 16 MB random-access memory was used for the numerical calculation which took ~ 40 minutes to complete. If one keeps the height z constant and takes the same raster for all measurements, then the matrix G and its inverse, G^{-1}, remain the same for all measurements. The inverse matrix was therefore stored and used in all subsequent analysis. The matrix multiplication [Eq. (3.6)] took only about 30 seconds. The inverse matrix G^{-1} occupied about 10 MB and 50 MB hard disk space when it was stored in binary and text formats respectively. After the magnetization M(i,j) is calculated, the sheet current can be obtained simply by taking the spatial derivatives of M using Eq. (3.1).

3.3.3. Iteration procedure

The magnetization M(i,j) can be also calculated by an iteration technique. This approach requires much less computer memory.

The induction $B_z(m,n,z)$ produced by the magnetic moments in the grid is given by Eq. (3.4). The iterative procedure started with appropriate initial values of the magnetization assigned to each grid point.

The far field of the magnetic moment decays as $\sim 1/r^3$, where r is the distance between the source and the field. Since the Hall probe was very close to the film

surface, it was natural to assume that the most significant contribution to the self-induction came from the magnetic moment of the grid cell directly beneath the field point. The initial values for the magnetization $M_0(i,j)$ were then estimated by using Eq. (3.4) without summations, i.e.,

$$M_0(i,j) = B_z(i,j,z) / G(i,j,i,j,z), \quad i,j = 1, \ldots, N, \tag{3.7}$$

where $B_z(i,j,z)$ is the measured self-induction (obtained by subtracting the applied induction from the measured induction). We now substitute the $M_0(i,j)$ for $M(i,j)$ in Eq. (3.4), i.e.,

$$B_{z0}(m,n,z) = \sum_{i=1}^{N} \sum_{j=1}^{N} G(m,n,i,j,z) M_0(i,j), \tag{3.8}$$

where $B_{z0}(m,n,z)$ is the calculated induction contributed from all grid cells associated with the initial magnetization M_0. At this stage, the calculated values B_{z0} are generally not in agreement with the measured B_z, the iterative values of M_0 are usually overestimated. The next step is to correct the values of M in order to improve the calculation. We substitute the difference between the measured and calculated induction, $\Delta B_z = B_z - B_{z0}$, into Eq. (3.7), which gives the correction term

$$\Delta M(i,j) = \Delta B_z(i,j,z)/G. \tag{3.9}$$

A new estimate for $M(i,j)$ is

$$M_1(i,j) = M_0(i,j) + \Delta M(i,j). \tag{3.10}$$

After inserting M1 into Eq. (3.4), one gets new values for the induction B_{z1}. The difference, $\Delta B_z = B_z - B_{z1}$, is then used to make the second correction. This procedure is repeated until the difference ΔB_z is less than a preset error limit. In practice, the above iteration procedure proceeds in such a way that ΔB_z decreases monotonically with the number of iterations. Typically, 30 iterations were needed to reduce $\Delta B_z/B_{max}$ to $\leq 0.1\%$, which is comparable to the experimental uncertainty. The corresponding computation time was approximately 1.7 minutes.

The memory required by the iteration program is proportional to N^2 (compared to N^4 in the matrix method) and therefore it is advantageous to use this method for data with a large number of grid points.

3.3.4. Testing the ideal case

The above two calculation procedures were tested using a prescribed current distribution. Let us consider a uniformly distributed current density, $j = 2.5 \times 10^6$ A/cm^2 (2.5×10^{10} A/m^2), over a 1.08×1.08 cm film, 300 nm thick. The current is assumed to flow in concentric square loops. The map of B_z generated by this current was calculated using the Biot-Savart law [Shortley and Williams 1965] at distance 250 μm above the film. Figs. 3.3(a) and 3.3(b) show the surface map and the corresponding contour map of the simulated field, respectively. To carry out the inverse calculation, both the matrix and iteration methods were used. The two methods gave exactly the same results, as shown in Fig. 3.3(c). The spatial distribution of M is in the form of a pyramid. Note that M = 0 outside the film, which corresponds to zero current outside the film, as expected.

The element of current paths (dx,dy) satisfies $dx/J_x = dy/J_y$. Using Eq. (3.1) leads to $(\partial M/\partial x)dx + (\partial M/\partial y)dy = 0$, and therefore the current paths follow the contour lines of M(x,y), M(x,y) = constant [see Fig. 3.3(d)]. For an ideal

superconductor (current paths follow concentric square loops) that leads to a pyramidal form of M(x,y) in agreement with the above inverse calculations. The value of the current is inversely proportional to the separation of the contour lines. Using Eq. (3.1) leads to J = 0.75 A/m; for d = 300 nm the density of current is J/d = 2.5×10^6 A/cm^2, which is in perfect agreement with the initially assumed value.

The calculations were repeated with an artificial noise introduced into the field map to simulate errors in the measurement. The main features of the unperturbed M were still maintained and the overall current density remained unchanged. Therefore we can conclude that our inverse calculation procedures were stable, and suitable for determining the induced currents in real superconducting thin films.

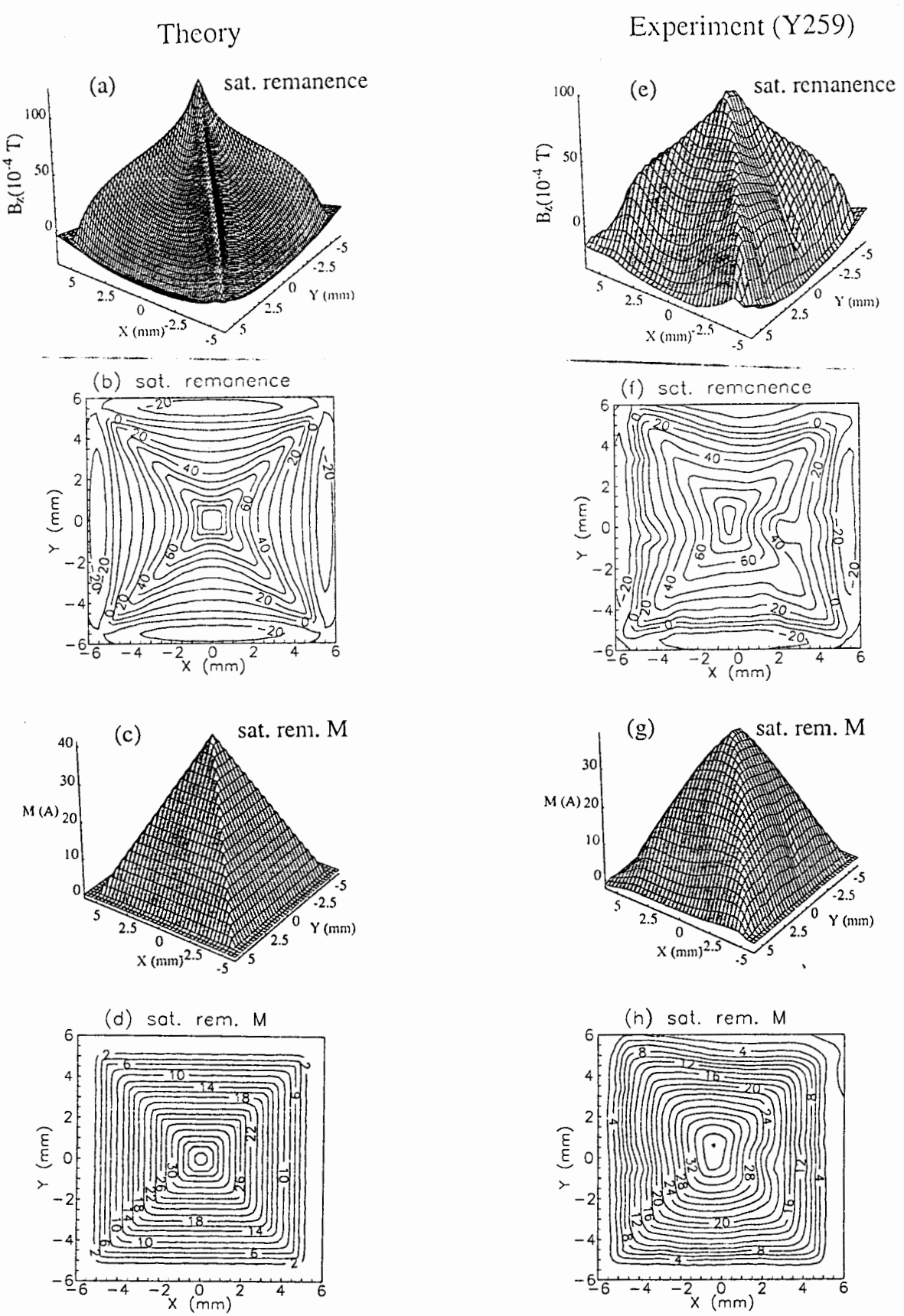

Fig. 3.3. Surface and contour maps of saturated remanent B_z and magnetization M for (a)-(d) the ideal and (e)-(h) the YBCO (Y259) thin-film samples, respectively.

3.4. Results and discussion: Full flux penetration

3.4.1. Remanent field

Figures 3.3(e) and 3.3(f) show surface and contour maps of the remanent B_z measurement with the Hall probe maintained at a typical distance of $z \approx 250$ μm above the film surface. The film was first zero-field-cooled to a stable temperature of 77 K, and then exposed to a large applied field H_a ($\mu_0 H_a \sim 30$ mT). After a few seconds, the field was removed. Figure 3.4 shows a particular line scan across the center of the film ($y = 0$). The B_z profile shows that the largest remanent induction B_z (≈ 9.4 mT) is located at the center of the film, indicating full flux penetration. The trapped flux is caused by vortex pinning in the film. The strength of the remanent flux density decreases gradually towards the edges and becomes negative in the vicinity of the edges with minima along the edges. The B_z profile approaches zero far away from the film. The most distinguishable feature in B_z maps of square-shaped films is a significantly enhanced trapped flux along the film diagonals, and that results in a typical X-shaped pattern. Along the sample diagonals the flux density is enhanced, creating distinct ridges, and between the diagonals it is noticeably concave [Fig. 3.3(e)]. This behavior is more evident in the contour plot of the remanent induction [Fig. 3.3(f)]. Defect sites are also clearly visible, they introduce noticeable deviations from the overall four-fold symmetry.

A negative trapped flux density around the sample edges is a consequence of sheet currents in thin samples such as films and disk-shaped samples [Frankel 1979]. On the other hand, the topological features of B_z are quite different for samples of different geometry.

The comparison between the remanent state maps of the YBCO film [Figs. 3.3(e) and 3.3(f)] and that simulated for an ideal film [Figs. 3.3(a) and 3.3(b)],

shows clearly a great deal of similarities. This is well demonstrated in the line scan along the x-axis which passes through the center of the film, see Fig. 3.4. The critical current density for an ideal sample, $j_{ideal} = 2.5 \times 10^6$ A/cm^2, was chosen to be approximately equal to the average critical current density of the YBCO film (see next section). Several conclusions can be reached from the above results: (a) the YBCO film is quite homogenous; (b) the currents follow concentric squares; and (c) the deviations from the perfect four-fold symmetry in the B_z map are caused by local imperfections of the film. Similar observations were found in our earlier measurements on TBCCO and YBCO thin films [Grant et al. 1994].

The flux penetration and trapped flux have been investigated in rectangular foils of Pb and In alloy [Huebener et al. 1969] and Nb [Rowe et al. 1971] by means of the magneto-optical effect using EuS-EuF_2 films. The authors [Huebener et al. 1969] believe that the trapped flux exhibits a Landau-like distribution, meaning that the trapped flux changes sign in individual domains. Our measurements show that their conclusion is incorrect, see Fig. 3.3(e).

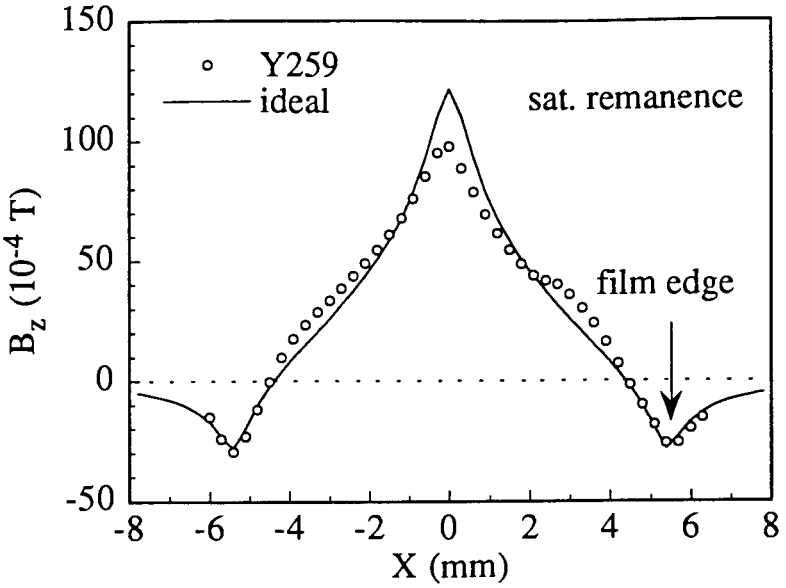

Fig. 3.4. Saturation remanent flux density B_z versus x for y = 0; open circles are measured B_z values of the YBCO film, and the solid line is the B_z profile of the ideal film calculated using $j_c = 2.5 \times 10^6$ A/cm^2.

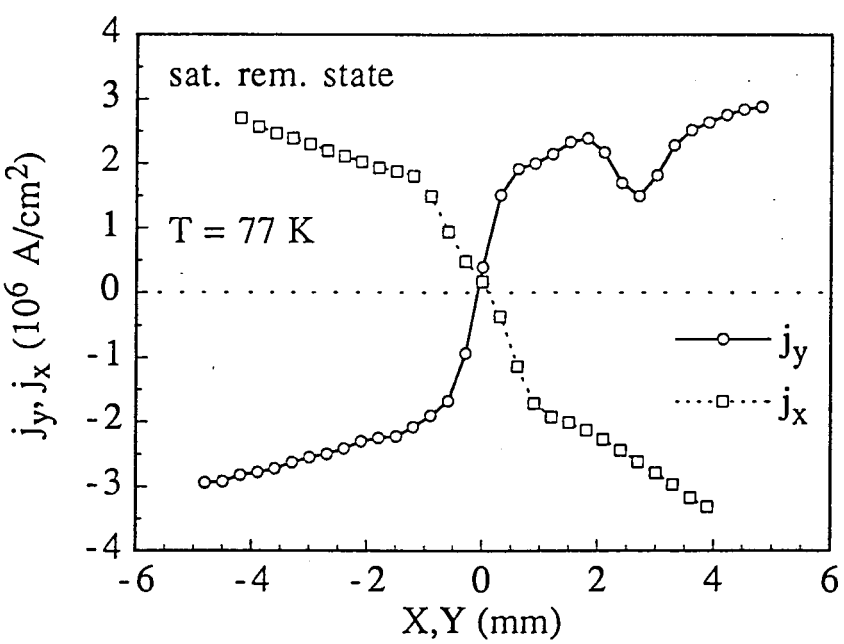

Fig. 3.5. Current density versus position for the YBCO film; open circles are $j_y(x)$ for y = 0, and open squares are $j_x(y)$ for x = 0. The lines are guides to the eye.

3.4.2. Magnetization and supercurrent

Figure 3.3(g) shows a surface map of the magnetization M of the YBCO film, which was directly calculated from the field measurement using the inverse matrix method. M(x,y) resembles very much the perfect pyramid of an ideal film, except that the corners are not as sharp. In regions outside the film, M was found to be zero as expected. The current distribution is represented by the contour lines of M [Fig. 3.3(h)]. It is evident that the current paths follow almost square loops.

Figure 3.5 shows two scans of current densities, j_y along the x axis and j_x along the y axis. This was done by taking the spatial derivatives of M [Eq. (3.1)] along the x and y directions for y = 0 and x = 0 respectively. Since the sample is nearly fully penetrated by the flux, the current will reach the local critical value everywhere except in the vicinity of the sample center [Campbell and Evetts 1972]. It is interesting to note that the value of j_c is not constant across the sample; i.e. $|j_y(x)|$ has the largest value (~ 3×10^6 A/cm^2) near the sample edge and decreases slightly toward the film center (~ 2×10^6 A/cm^2). In the vicinity of the film center, the current density changes rapidly in sign. The influence of rapid variations in the current distribution on the measured field B_z gets weaker with increasing distance from the film surface and could be partly lost in the instrumental noise. Since the measurements were carried out 250 μm above the sample surface, the calculated current distribution around the center of the film is broadened as is evidenced in Fig. 3.5. Around x = 3 mm, $j_y(x)$ shows a local minimum demonstrating the dependence of j_c on sample defects.

In the case of full flux penetration, the remanent flux density is largest at the film center and decreases rapidly toward the edge, and therefore the observed slow decrease in j_c with the distance from the sample edge, see Fig. 3.5, is very likely caused by the dependence of j_c on the local flux density. This also explains

the lower peak value of the remanent induction for the YBCO film, compared with that of the ideal film (see Fig. 3.4). The smaller j_c values ($< j_{ideal} = 2.5 \times 10^6$ A/cm^2) in the central region of the YBCO film result in decreased values of B_z in that region. The dependence of j_c on the flux density will be discussed in more detail in Section 3.5.2.

The value of the zero-field critical current density at 77 K ($\sim 3 \times 10^6$ A/cm^2) is in good agreement with that obtained from measurements using inductive techniques [Xing et al. 1993]. The large value of j_c suggests the existence of strong vortex pinning in the measured YBCO films.

3.4.3. Saturation magnetization

A few interesting characteristics of the sheet magnetization M are worth pointing out. The maximum value of the volume magnetization M_{vol} (M_{vol} = M/d), is of the order of 10^7 A/m. The peak value of $\mu_0 M_{vol}$ is about 100 T, which is four orders of magnitude greater than the value of the measured B_z ($\sim 10^{-2}$ T). The large value of M_{vol} is caused by the large value of the supercurrent density j. The flux density B_z is continuous across the film boundary, and therefore the measured B_z (which is very close to the film surface) should be nearly the same as B_z inside the sample. The definition $B_z = \mu_0(H_z + M_{vol})$ implies that inside the film $H_z \approx -M_{vol}$, as one would expect for the demagnetization factor in this geometry. The magnetization vector M(x,y) produces surface charge on both sides of the film; the condition $H_z(x,y) \approx -M_{vol}(x,y)$ implies that the internal demagnetizing field, $H_z(x,y)$, at any point inside the film is, in the first approximation, given by the demagnetizing field of an infinite sample with a homogeneous surface charge corresponding to the local magnetization M(x,y). However the variations of the magnetic charge [$\pm$M(x,y)] across the film are

essential because they are solely responsible for the spatial variations of the measured small flux density B_z outside the film.

Figure 3.3(g) shows that the distribution of the magnetization, M(x,y), of the measured YBCO thin film was close to the ideal pyramid of Fig. 3.3(c). Since in this case the critical current flows nearly everywhere in the sample, M represents the saturation magnetization. The total magnetic moment m, which can be measured with a magnetometer, is given by the integration of M over the film area. For a square-shaped, homogeneous type-II superconducting thin film, the saturation moment m_{sat} is equal to the volume of the magnetization pyramid $V_{pyr} = 4J_c a^3/3 = j_c aV/3$, where 2a is the length of the film edge and $V = (2a)^2 d$ is the volume of the sample, and therefore the averaged saturation volume magnetization M_{sat} is

$$M_{sat} = \frac{V_{pyr}}{V} = \frac{j_c a}{3}. \tag{3.11}$$

The same saturation magnetization is found for disc and cylindrical samples of radius a [Bean 1962 and 1964; Däumling and Larbalestier 1989; Mikheenko and Kuzovlev 1993; Zhu et al. 1993; Clem and Sanchez 1994a].

A direct numerical integration of the calculated M, derived from the field patterns of the YBCO film, gave $M_{sat} = 5.3 \times 10^7$ A/m. On the other hand, the ideal film ($j_{ideal} = 2.5 \times 10^6$ A/cm^2 and a = 0.54 cm), whose induction profile showed good agreement with that of the YBCO film (see Fig. 3.4), gave $M_{sat} = 4.5 \times 10^7$ A/m. The two values are in good agreement considering the fact that the critical currents in the measured film are somewhat dependent on the local flux density.

3.5. Results and discussion: Partial flux penetration

At 77 K, partial flux penetration takes place when the applied flux density $\mu_0 H_a$ is less than 10 mT.

3.5.1. Field mapping

A series of field measurements was carried out in order to observe the process of flux penetration. The sample was initially zero-field-cooled. Field mapping was first carried out in the presence of an applied flux density $\mu_0 H_a = 4$ mT, followed by the second field mapping at $\mu_0 H_a = 8$ mT. H_a was then switched off and the remanent field mapping was carried out. The field maps are shown in Figs. 3.6(a)-3.6(c). The corresponding field contour plots are shown in Figs. 3.6(d)-3.6(f).

The results obtained for a low field ($\mu_0 H_a = 4$ mT) [Figs. 3.6(a) and 3.6(d)] show that the flux enters deeper at the middle of the film edges than in the corners, which results in a concave surface in the field map. The magnetic induction B_z is zero in a central square-like region of the film, due to the complete shielding effect of the induced current, see Fig. 3.6(d). The supercurrent contribution to B_z outside the film is in the same direction as the applied flux density B_a. This demagnetizing effect leads to an appreciable enhancement of B_z around the film edges, see Fig. 3.6(d). The magnetic surface charge [M(x,y)] depends on the state of flux penetration (or trapped flux) and it leads in general to a nonuniform distribution of demagnetizing fields. When the magnetic flux is nearly excluded from the sample, the concept of a uniform demagnetizing field is useful [Goldfarb et al. 1992]. For thin films the demagnetizing factor is close to one and that leads to increased magnetic flux density around the film edges. However, in the general case, one cannot treat the

demagnetizing fields by a constant demagnetizing factor; the full distribution of the sheet magnetization (magnetic charge) has to be employed.

The field distribution measured with the applied flux density $\mu_0 H_a = 8$ mT [Figs. 3.6(b) and 3.6(e)] shows that the leading flux front evolves symmetrically from the middle of the four edges toward the center of the film. This leaves the diagonal regions with a relatively low flux density. This is exactly opposite to the saturated remanent case in which the trapped flux is enhanced along the diagonals, see Figs. 3.3(e) and 3.6(f). These two cases show that it is easier for flux lines to enter and exit the film from the middle of the film edges than from the corners. One should note that there is still a small flux-free region in the very center of the film. The overall flux penetration in thin films appears to have an X shaped pattern. This behavior has been commonly observed in magneto-optical images of HTS thin-film samples [Indenbom et at. 1990; Brüll et al. 1991; Brown 1994].

The remanent induction B_z [Figs. 3.6(c) and 3.6(f)] shows clearly local minima along the diagonals. Notice the negative remanent induction around the edges. The flux is trapped in four quadrants divided by the diagonals, resulting in four hills.

Flux penetration in the perpendicular configuration is a unique problem for 2D superconductors [Clem and Sanchez 1994a]. A zero-field-cooled sample tries to shield an applied field $|H_a| > 0$ inside the sample by inducing screening supercurrents. Due to strong demagnetizing effects, the magnetic field outside the film edge is greatly enhanced by $\sim (a/d)H_a$ for a circular thin film [Goldfarb et al. 1992]. When H_a is larger than $(d/a)H_{c1}$, the local magnetic field at the film edge will exceed H_{c1}. According to the critical state model [Campbell and Evetts 1972], vortices penetrate only as far as necessary to reduce the magnitude of the

local current density to its critical value. The depth to which the vortices penetrate depends upon the strength of vortex pinning in the sample.

It is interesting to compare the distribution of the induction in the remanent state [Figs. 3.6(c) and 3.6(f)] and in the state corresponding to the originally applied flux density $\mu_0 H_a = 8$ mT [Figs. 3.6(b) and 3.6(e)]. One can see that in the inner region of the film (from the center to the hill-tops) the flux distribution is similar. The only difference between these cases is in the outer region where, for the remanent state, the field rapidly drops as it approaches the film edges.

The local minima of B_z along diagonals in the remanent state change to local maxima for sufficiently high applied fields. In the latter case the sample is fully penetrated by the flux. The maximum trapped flux density B_{max} is observed above the center of the sample. In order to reach the saturation remanent state, one needs to apply an external flux density $B_a \geq 2B_{max}$.

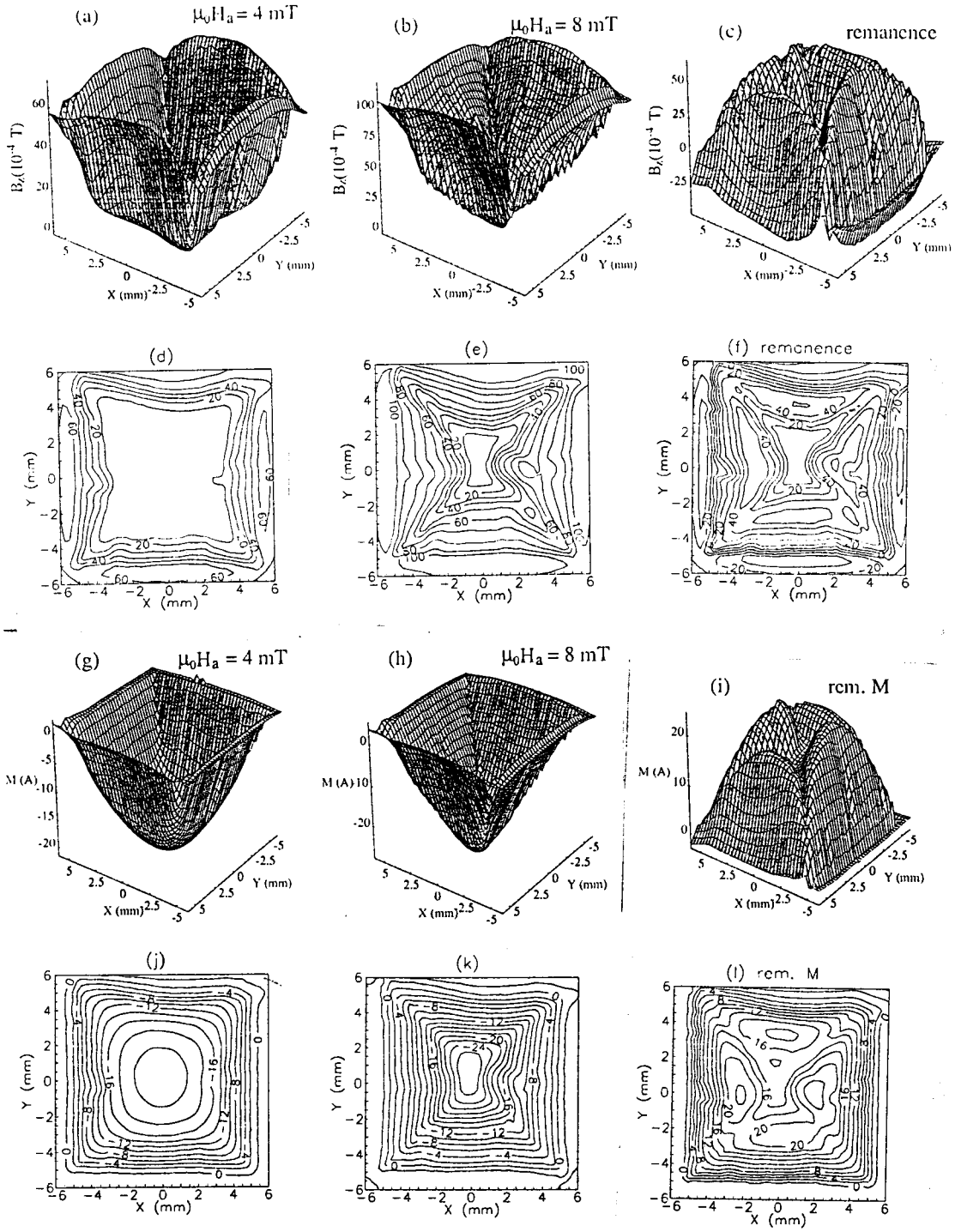

Fig. 3.6. Surface and contour maps of B_z (a)-(f) and M (g)-(l) of the YBCO film for sequentially applied external fields: $\mu_0 H_a = 4$ mT, 8 mT, and zero mT (after the previous state $\mu_0 H_a = 8$ mT).

3.5.2. Magnetization and current patterns

We have used the same experimental arrangement for all field measurements and therefore the stored inverse matrix $\mathbf{G}^{-1}$ was calculated only once. The magnetization distributions M(x,y) for the measurements in sequentially applied fields $\mu_0 H_a$ = 4 and 8 mT, and 0 T (remanent state from the previous state $\mu_0 H_a$ = 8 mT) are obtained by a simple matrix multiplication [Eq. (3.6)], see Figs. 3.6(g)-3.6(i), respectively. The corresponding current distributions (contour plots of the M's) are shown in Figs. 3.6(j)-3.6(l). The values of the current density were evaluated from Eq. (3.1) and are shown as a function along the axis x for y = 0 in Figs. 3.7(a)-3.7(c).

For a relatively small applied flux density $\mu_0 H_a$ = 4 mT, the current within the depth of the field penetration is parallel with the edges and makes sharp turns at the corners showing clear square-like patterns, see Fig. 3.6(j). In the inner part of the film where the external induction is compensated by the self-induction, the current loops are rounded. The roundness increases upon approaching the center of the sample. Near the center one can see a well defined circle [see Fig. 3.6(j)]. The plot of j_y versus x [Fig. 3.7(a)] for y = 0 shows that $j_y(x)$ reaches the critical value j_c (field dependent) in the outer region of the film where the flux penetrates and gradually decreases to zero toward the center. It follows that the current has a tendency to follow circular and square patterns in the flux free and flux penetrated regions respectively. The presence of screening currents ($j < j_c$) in the flux free region is a general property of thin samples, e.g. see the distribution of current in a disk-shaped geometry [Mikheenko and Kuzovlev 1993; Zhu et al. 1993; Clem et al. 1994]. The supercurrents change from critical values to zero gradually, contrary to the simple Bean model [Bean 1962, 1964], where the supercurrents are either critical or zero.

In the measurements with field on (B_a = 4, 8 mT) one can see again the effect of the field dependence of j_c. In this case the situation is reversed relative to that for the remanent state; the flux density B_z decreases from the maximum value at the film edge to zero in the inner part of the film. Consequently (within the depth of the flux penetration), $|j_c|$ increases when moving from the film edge to the center.

At $\mu_0 H_a$ = 8 mT, the flux penetrates noticeably further into the sample [see Fig. 3.6(h)], so that a large part of the film carries the current which reaches the local critical value [Fig. 3.7(b)]. The defect sites are quite visible; the current flows around them to maintain a continuous path. The effect of the field dependence of j_c is more clearly seen from the $j_y(x)$ curve, see Fig. 3.7(b). The corners of the current loops are somewhat stretched outwards along the diagonals, see Fig. 3.6(k). This feature is also visible for $\mu_0 H_a$ = 4 mT and for the remanent state [Figs. 3.6(k) and 3.6(l)], but it is absent for the case of full field penetration [Fig. 3.3(h)]. Brüll et al. speculated about a possibility of stretching the sheet currents along the sample diagonals [Brüll et al. 1991], and they argued that the current stretching along the diagonals enhances the strength of the self-induction along diagonals (demagnetizing field); therefore the flux shielding would become more effective in these regions. However our measurements showed that the above stretching of the sheet currents along the sample diagonals is much less pronounced than suggested by Brüll et al., see Fig. 3.6(k).

Figures 3.6(i) and 3.6(l) show the remanent M map and its contour map for the initially applied flux density $\mu_0 H_a$ = 8 mT. Similar to the remanent field map [Fig. 3.6(c)], the map of the remanent M is divided into four symmetric hill tops. At the outer periphery, the currents flow in large loops which are approximately parallel to the edges, and around the hill tops the currents flow in closed loops, see in Fig. 3.6(l). This multiply-connected current distribution in Fig. 3.6(l) is

caused by the rearrangement of supercurrents, after the applied field is removed. Figure 3.7(c) shows that, within the region where the change of the flux density is more rapid (from the hill tops to the specimen edges), the induced current is saturated and hence critical. The critical current also changed its direction compared to the initial state with $\mu_0 H_a$ = 8 mT, as expected. The field distribution from the hill top to the center of the sample is not much changed compared to that in the applied field, see Figs. 3.6(e) and 3.6(f). However the current distribution in this region is very strongly affected [compare Figs. 3.6(k) and 3.6(l)]. In an unsaturated remanent state the field in the central region of the specimen is zero, and therefore the closed current loops have to be present in order to compensate the field from the currents which circulate around the sample edges.

The induction **B** in thin films has components $B_{x,y}$ and B_z which are tangential and perpendicular to the film surface, respectively. B_z was described in Section 3.3.1. $B_{x,y}$ can be derived from Ampere's law, $\nabla \times \mathbf{B} = \mu_0 \mathbf{j}$. Our measurements of $B_z(x,y)$ showed [Grant et al. 1994] that the contribution of $\partial B_z/\partial x,y$ to Amperes law is much smaller than that of $\partial B_{x,y}/\partial z$, and therefore $B_{x,y} \sim \mu_0 J_{tot}/2$. J_{tot} is the integrated total current over the thickness of the film (per unit length along the sample surface). $B_{x,y}$ is oriented perpendicular to the sheet current. Its direction is opposite at the top and bottom sides of the film surface, and by symmetry, the field $B_{x,y}$ is zero in the middle of the film. It is only the component B_z which generates the in-plane Lorentz force [Clem 1994b], which is balanced by the pinning force of vortex traps; and therefore one can expect that j_c is dependent only on B_z. More detailed discussions will be given in Chapter 4.

Figure 3.8 shows the current density j_c as a function of the local flux density B_z at the temperature T = 77 K. The j_c value decreased by a factor of 1.7 as B_z

increased from 0 to 10 mT. Kim's theoretical model [Kim et al. 1962] for $j_c(B_z)$ gives

$$j_c(B_z) = \frac{j_c(0)}{1 + B_z/B_0}. \tag{3.12}$$

When this is applied to the data, it is found that $B_0 \approx 15.7$ mT, and $j_c(0) = 3 \times 10^6$ A/cm^2.

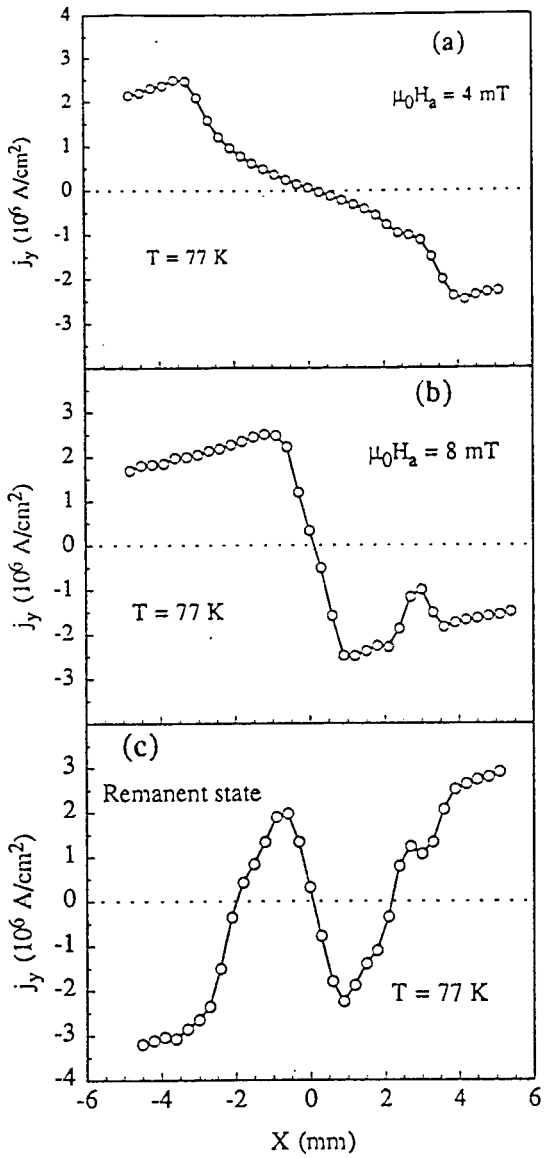

Fig. 3.7. j_y versus x for y = 0 for the YBCO film (a) $\mu_0 H_a$ = 4 mT, (b) $\mu_0 H_a$ = 8 mT, and (c) remanent state. The solid lines are guides to the eye.

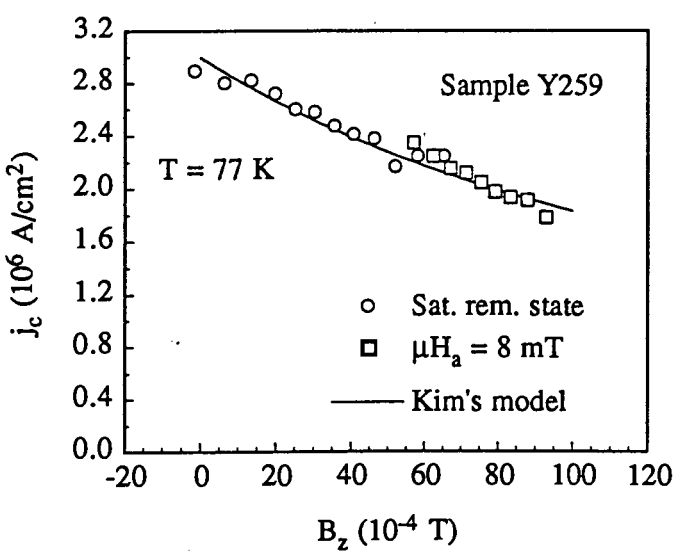

Fig. 3.8. j_c versus B_z for the YBCO film; open circles are j_c values in the saturation remanent state, and open squares are for $\mu_0 H_a$ = 8 mT. The solid line is a Kim model fit: $j_c(0) = 3 \times 10^6$ A/cm^2 and $B_0 \approx 15.7$ mT.

3.6. Superposition principle

In this section, we will show that the above multiply-connected current patterns in the remanent state can be reconstructed from the superposition of two singularly-connected current patterns.

3.6.1. General relations

The hysteresis cycle of a type-II superconductor (for H_a varying between $\pm H_0$, where H_0 is the extremal applied field) can be calculated by using a linear superposition principle. This calculation has been applied to strip- and disk-shaped geometries [Brandt et al. 1993; Zhu et al. 1993] and was summarized by Brandt et al. [1993] in concise formulas. The linear superposition principle relates a physical quantity such as the magnetization $M\downarrow$ for H_a on the descending part of the hysteresis loop with appropriate states along the so-called "virgin" magnetization cycle (H_a from 0 to H_0). The expression for $M\downarrow$ is then given by

$$M\downarrow(x,y,H_a,J_c) = M(x,y,H_0,J_c) + M(x,y,H_a - H_0,-2J_c). \qquad (3.13)$$

Similar relations are valid for the current density J (or j) and the self-induction B. One can expect that the topological features (x-y dependence) of M are dependent only on the ratio H_a/H_c, where H_c is the characteristic field which is proportional the critical current density ($\sim J_c$). However the magnitude of M is expected to scale directly with J_c, therefore

$$M(x,y,H_a,J_c) = H_c F(x,y,H_a / H_c). \qquad (3.14)$$

This relationship was rigorously proven to be valid for narrow strip and disk geometries [Brandt et al. 1993; Zhu et al. 1993]. The same relations also hold for the current J (or j) and the self-induction B. Equations (3.13) and (3.14) were used to reconstruct the distributions (hysteresis) of B_z, M, and j_y for the remanent state.

3.6.2. Application

We now apply the above formulas to the case of a square-shaped YBCO thin film. Let $\mu_0 H_a = 0$ and $\mu_0 H_0 = 8$ mT. Then, $M_\downarrow$ on the left-hand-side of Eq. (3.13) becomes the remanent magnetization. The first term on the right-hand-side of Eq. (3.13) corresponds to the magnetization in the applied field of 8 mT. Using the scaling relation (3.14), we can rewrite the second term on the right-hand-side of Eq. (3.13) as

$$M(x,y,-H_0,-2J_c) = -2H_c F(x,y,H_0/(2H_c)). \tag{3.15}$$

A simple inspection of Eq. 3.15 shows that the function $F(x,y,H_0/(2H_c))$ (describing the topography of M) can be found from the measurements on the sample which has the same critical field H_c (the same current j_c) but in the applied field $H_a = H_0/2$,

$$M(x,y,-H_0,-2J_c) = -2M(x,y,H_0/2,J_c). \tag{3.16}$$

For the above remanent state the magnetization $M(x,y,H_0/2,J_c)$ in Eq. (3.15) is given by the Hall probe measurements taken at $\mu_0 H_a = 4$ mT along the virgin path.

Figures 3.9(a) and 3.9(b) show the surface and contour maps of the remanent flux density B_z constructed from the two virgin B_z distributions for $\mu_0 H_a = 4$ and 8 mT, using Eqs. (3.13) and (3.16). Within the experimental uncertainty, the constructed field map resembles well the experimentally measured field map B_z in the remanent state, see Figs. 3.6(c) and 3.6(f). The same agreement is also found between the constructed and measured remanent magnetizations, see Figs. 3.9(c), 3.9(d) and Figs. 3.6(i) and 3.6(l), respectively. The constructed remanent current density $j_y(x)$ is shown in Fig. 3.10. It agrees well with the measured $j_y(x)$, except at the film edges. Notice that at the film edges, the values of B_z are different for the two cases. This discrepancy is a consequence of the field dependent j_c. However the overall agreement between the measured results and those obtained by means of the above superposition principle suggests that this method can be used very effectively for any part of the hysteresis loop. The method is useful for the understanding of screening currents in various parts of the cycle. In particular it helps to understand the multiply-connected remanent current distribution in terms of two simply-connected virgin current distributions. For example, the prefactor –2 in the second term of Eq. (3.16) doubles the value of the current, and that results, as expected, in the reversal of the direction of the current around the film edges.

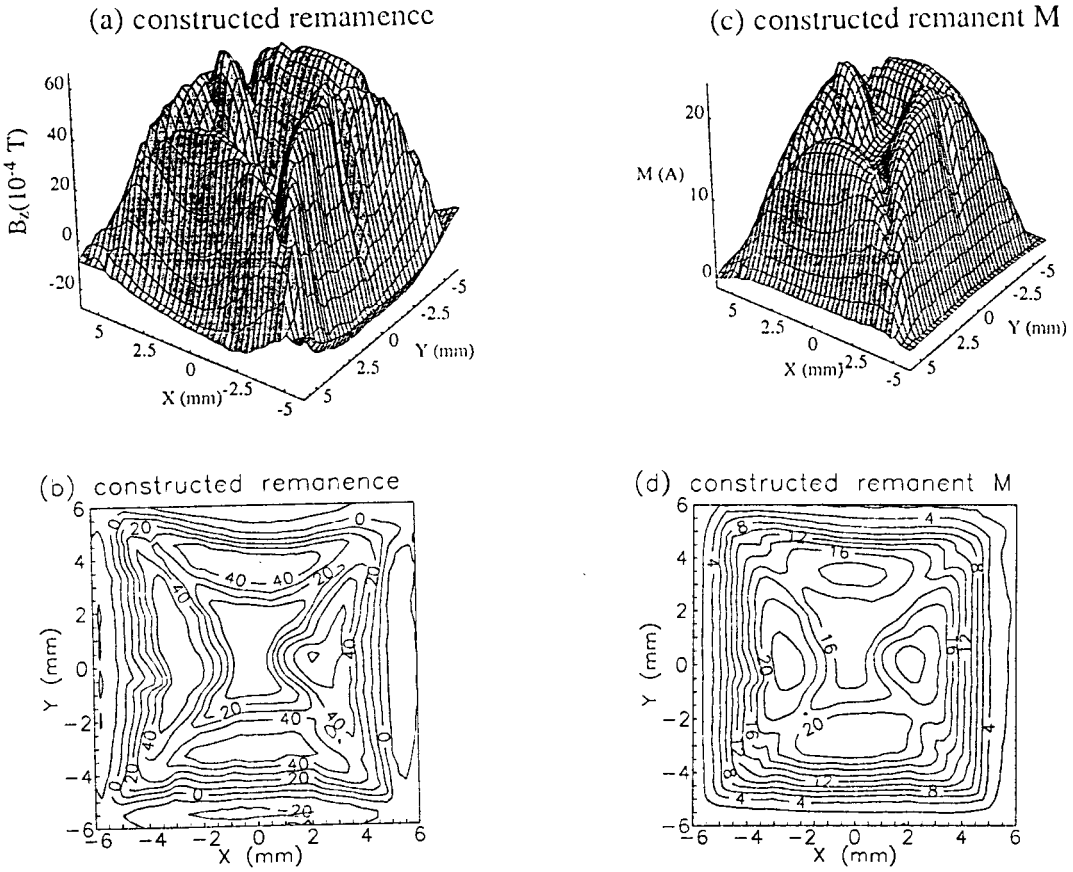

Fig. 3.9. Surface and contour maps of reconstructed remanent (a)-(b) B_z and (c)-(d) magnetization M ($\mu_0 H_a$ reduced to zero from 8 mT). Compare Figs. 3.6(c), (f) and 3.6(i), (l).

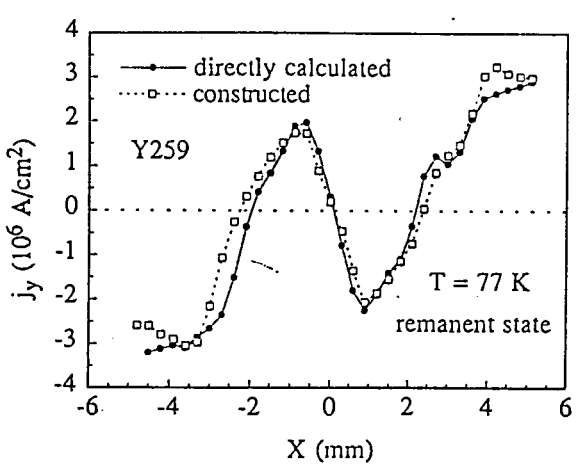

Fig. 3.10. j_y versus x for y = 0 for the YBCO film in the remanent state ($\mu_0 H_a$ reduced to zero from 8 mT); solid circles are j_y values directly calculated from M, and open squares are reconstructed j_y values using the superposition principle. The solid and dashed lines are guides to the eye.

3.7. Conclusions

A scanning micro-Hall probe was used to map the local flux density B_z at a height $z \approx 250$ μm above the surface of a YBCO thin film. Numerical calculation procedures were developed by employing the spatially varying sheet magnetization M to obtain the current distribution and absolute values of the critical current densities from the measured field maps. The calculated current distributions for various applied fields demonstrate: (a) The current path closely follows the sample's geometrical shape, when a zero-field-cooled thin-film sample is fully penetrated by the applied field H_a perpendicular to the film surface. (b) The current path is different in the flux free region, when the sample is only partially penetrated by an applied field. In this region circular current loops are formed and the value of the screening current decreases to zero as the center of the film is approached. (c) The critical current loops are slightly stretched peripherally. This effect is particularly pronounced for moderate applied fields and leads to a very effective shielding along the sample diagonals.

We have shown that the linear superposition relations suggested for the hysteresis cycle of type-II superconductors are applicable for square-shaped thin-film samples. The application of these relations shows that the measured complex, multiply-connected remanent current patterns can be reconstructed by the superposition of two simple singularly-connected current distributions.

We have demonstrated that the scanning micro-Hall probe technique can provide quantitative, detailed information over the whole sample under inspection. The following features are particularly important: (a) The ability to determine the current distribution (including J_c) in superconducting thin-film samples of arbitrary geometries in a non-destructive manner. Since the field measurement is absolute, the Hall probe can be used to calibrate other measurement techniques, such as the screening technique [Xing et al. 1993]. (b)

The capability to identify the presence and locations of various defects in the superconducting film. This information is critical for device applications. The micro Hall probe maps can be used to select suitable superconducting films and determine the appropriate areas for device fabrication. (c) The capacity to investigate the processes of flux penetration and current flow, which are fundamental to the understanding of the critical state in type-II thin-film superconductors.

Chapter 4
Spatial Distributions of Total Magnetic Flux Density

4.1. Introduction

The previous chapter showed that the sheet magnetization M(x,y) and the sheet current J(x,y) can be obtained from the distribution of the normal component of the magnetic flux density, B_z, measured by a scanning micro-Hall probe. The transformation from the B_z map to the sheet current map involves the process of inverse calculation. We now show that, given the distribution of M(x,y) or J(x,y), one can calculate the flux density **B** anywhere around the film, including the tangential components of **B**, B_x and B_y, which are not obtainable directly from our scanning Hall Probe measurements. This is a straightforward calculation problem which does not require a large amount of computer time.

For a known distribution of local sheet magnetization **M**(i,j), the magnetic flux density **B** at a point (m,n,z) is given by the general formula [Jackson 1975]

$$\mathbf{B}(m,n,z)=\frac{\mu_0}{4\pi}\sum_{i,j=1}^{N1,N2}\int_{S_{i,j}}\frac{3\mathbf{r}[\mathbf{r}\cdot\mathbf{M}(i,j)]-r^2\mathbf{M}(i,j)}{r^5}dx'\,dy', \tag{4.1}$$

where the integral is taken over the grid cell (i,j), see Fig. 3.2. Recall that **M** has only the normal component M. Equation (4.1) gives both the perpendicular component B_z, see Eq. (3.4), and the tangential components $B_{x,y}$,

$$B_x(m,n,z)=\frac{\mu_0}{4\pi}\sum_{i,j=1}^{N1,N2}M(i,j)\int_{S_{i,j}}\frac{3xz}{r^5}dx'\,dy', \tag{4.2a}$$

$$B_y(m,n,z)=\frac{\mu_0}{4\pi}\sum_{i,j=1}^{N1,N2}M(i,j)\int_{S_{i,j}}\frac{3yz}{r^5}dx'\,dy'. \tag{4.2b}$$

The flux density **B**(m,n,z), is valid anywhere in the space outside the film. One can thus calculate the spatial distribution of the flux density **B** anywhere around the thin-film sample, except very close to the surface of the film. (The limitation of the distribution height of **B** will be discussed later.) This will give a full picture of magnetic flux penetration or trapping in the vicinity of the thin-film sample.

4.2. Results and discussion: Saturation remanent state

4.2.1. Tangential components

Figures 4.1(a) and 4.1(b) show the distributions of the tangential component B_x, calculated by using Eq. (4.2), for an ideal film and for a YBCO film (Y259), respectively. The ideal film has uniformly distributed, concentric, square current loops. The current distribution or the magnetization of the YBCO film was obtained from the inverse transformation procedure described in the previous chapter, see Fig. 3.3. The B_x maps shown in Fig. 4.1 are at a distance $z = 250$ μm above the film surface. This height is the same as that of the flux mapping for the YBCO film. The B_x map for the YBCO film corresponds to the trapped flux at 77 K. The micro-Hall probe measurements were carried out at the same temperature. The external magnetic field was aligned perpendicular to the film surface.

The tangential components B_x for both films are distributed over two opposing triangles. B_x has an opposite sign in the two regions. The sample symmetry requires that the component B_y is distributed in two other triangles, orthogonal to those with the B_x distributions. As a result, there are either $B_{x,z}$ or $B_{y,z}$ components of **B** in the neighboring triangular regions. Along the film

diagonals, both B_x and B_y vanish, see Fig. 4.1, while B_z shows local maxima in these regions, see Fig. 3.3. Figure 4.1(c) shows the $B_x(x)$ profiles along a line across the film ($y = 0$) for both the YBCO film and for the ideal film.

The overall profiles of the tangential flux density for the YBCO film and for the ideal film are very comparable. However, the field-independent critical currents in the ideal film generate nearly constant B_x values over a large part of the triangular region, see Figs. 4.1(a) and 4.1(c). On the other hand, a noticeable slope in $B_x(x,y)$ for the YBCO film, see Figs. 4.1(b) and 4.1(c), reflects the dependence of critical currents on the internal flux density B_z. Note that the trapped flux density was highest and the critical current was lowest in the middle of the film. The kinks seen in the B_x map of the YBCO film demonstrate the presence of sample defects.

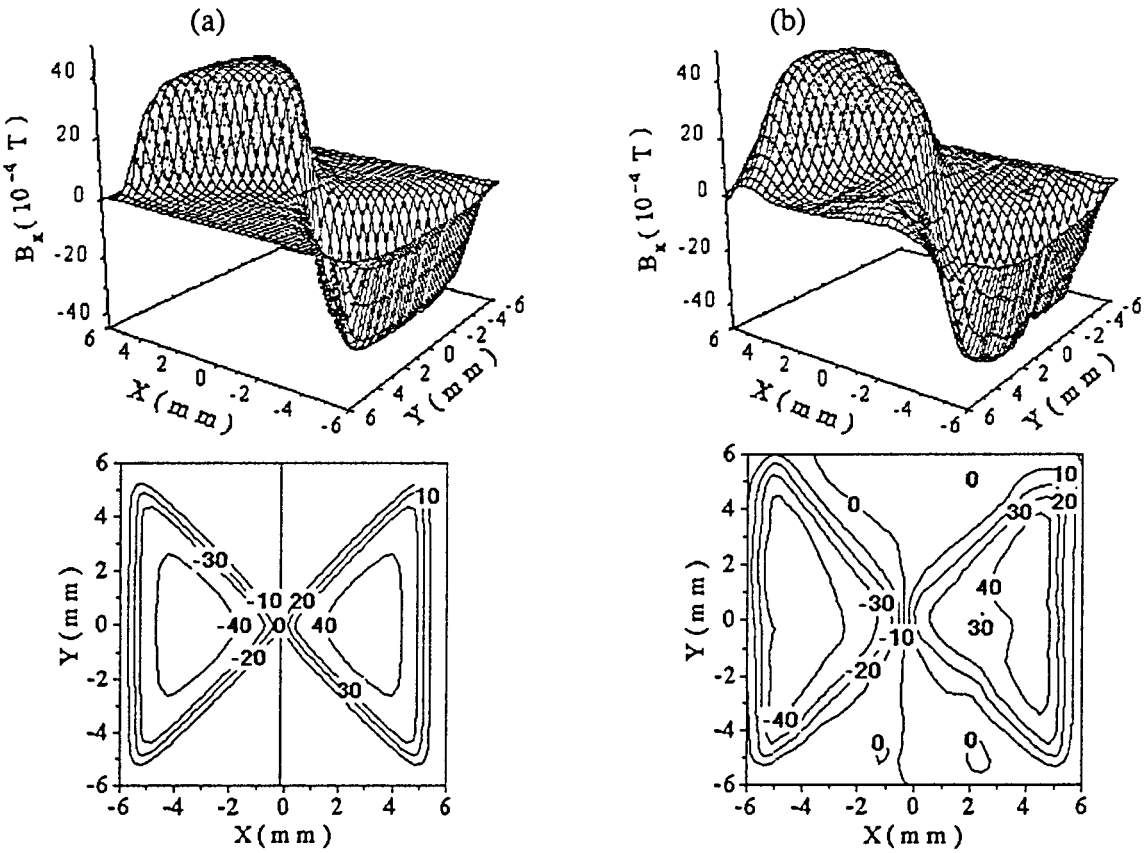

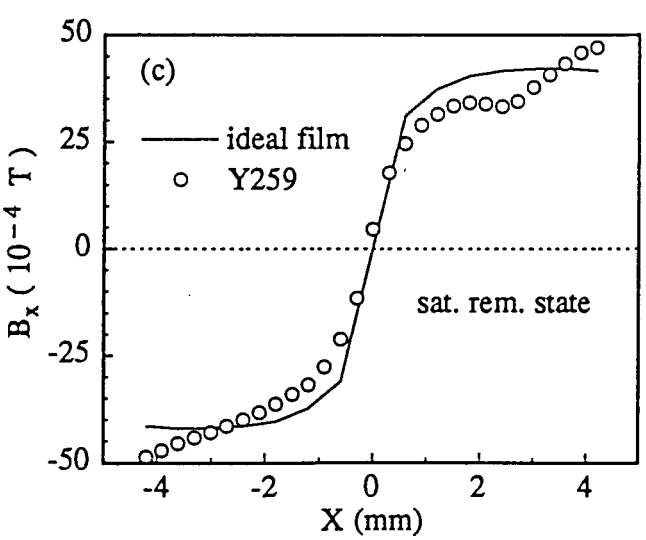

Fig. 4.1. Distributions of the tangential flux density B_x for (a) an ideal film and (b) a YBCO thin film. (c) B_x versus x for y = 0.

4.2.2. Validity of the forward calculation

The calculations shown in Fig. 4.2 demonstrate the dependence of B_x and B_z on the grid size, w, of the sheet magnetization M(x,y). The finite grid size w originates from the finite scanning step of the flux mapping measurement. The normal component $B_z(z,w)$ was calculated at the film center. The tangential component $B_x(z,w)$ was calculated at midway between the center and the edge of the film. Several different grid sizes were used in the calculation: w = 0.02, 0.15, and 0.3 mm. For $z > w$ the B_x values are independent on the grid size. For $z < w$ the B_x decreases with a decreasing z and approaches zero for $z \rightarrow 0$. This is an artifact of the finite grid size. The Maxwell equations (Ampere's law) predict that B_x reaches a constant value by approaching the film surface, see detailed discussions below, and changes its sign in the mid-plane of the film. Obviously the calculations for $z \rightarrow 0$ lead to the average value of B_x through the sample thickness, $B_{x,av} = 0$. The calculated values of B_z support that view. B_z is continuous across the film thickness and the calculated B_z shows little dependence on z even for $z < w$.

4.2.3. Application of Ampere's law

Ampere's Law

$$\oint \mathbf{B} \cdot d\mathbf{l} = \mu_0 I \qquad (4.3)$$

was applied to the integral path shown in Fig. 4.3. The integral path is in x-z plane which encloses a section of sheet current J_y (= $j_y d$, where j_y is the current density) whose direction is indicated by crosses in the thin-film superconductor. Equation (4.3) then becomes

$$\frac{\Delta B_x}{d} + \frac{\Delta B_z}{\ell}\frac{t}{d} = \mu_0 j_y, \tag{4.4}$$

where ℓ and t are the integral paths along the x and z directions respectively, ΔB_z is the difference in B_z values at locations separated laterally by ℓ, and ΔB_x is the difference between the B_x values above and below the film (separated by a distance t), see Fig. 4.3. Since the film thickness d is comparable to 2λ, where λ is the London penetration depth, the current density j is considered uniform over the film thickness. (Otherwise, j is the average value over the film thickness.) The first term in (4.4) is due to the curvature of **B**, ($B\nabla \times \hat{\mathbf{B}}$, where $\hat{\mathbf{B}}$ is the unit vector along $\mathbf{B} = B\hat{\mathbf{B}}$) and the second term is due to the gradient of B, ($\nabla B \times \hat{\mathbf{B}}$) [Clem 1994b]. Since B_x and B_z are comparable (see Fig. 4.2) and t can be close to d, the second term (due to the gradient of B) is much smaller than the first term (due to the curvature of **B**) ($\ell \gg$ d). For example, taking $\ell \approx 1$ mm and d ≈ 0.3 μm, we estimated that the gradient term is approximately three orders of magnitude smaller than the curvature term. Therefore, Eq. (4.4) becomes

$$\frac{\Delta B_{x,y}}{d} = \frac{2B_{x,y}}{d} \approx \mu_0 \left| j_{y,x} \right|, \tag{4.5}$$

where $\Delta B_{x,y} = 2B_{x,y}$.

Equation (4.5) shows that the current density j in thin film geometry is mostly determined by the curvature of **B**, which is in strong contrast with the situation in a long cylindrical superconductor with an axial applied field, where the shielding current is determined solely by the gradient of B [Bean 1962, 1964]. The same conclusion was reached by Clem [1994b] using different arguments.

As an example, we estimate the B_x value at the film surface using Eq. (4.5), assuming a local current density $j = 3 \times 10^6$ A/cm^2 which corresponds to the j_c

value at $x \approx -4$ mm in Fig. 4.1(c). It turns out that the B_x value at the film surface is only about 13% larger than that at a distance $z = 250$ μm above the film surface, see Fig. 4.1(c). In fact, the profile of the $B_x(x)$ curve in Fig. 4.1(c) is very similar to that of $j_y(x)$ for the YBCO film, see Fig. 3.5. This observation confirms the validity of Eq. (4.5) and shows clearly that the local current density in superconducting thin films is determined by the tangential components of **B** at the surface of the film.

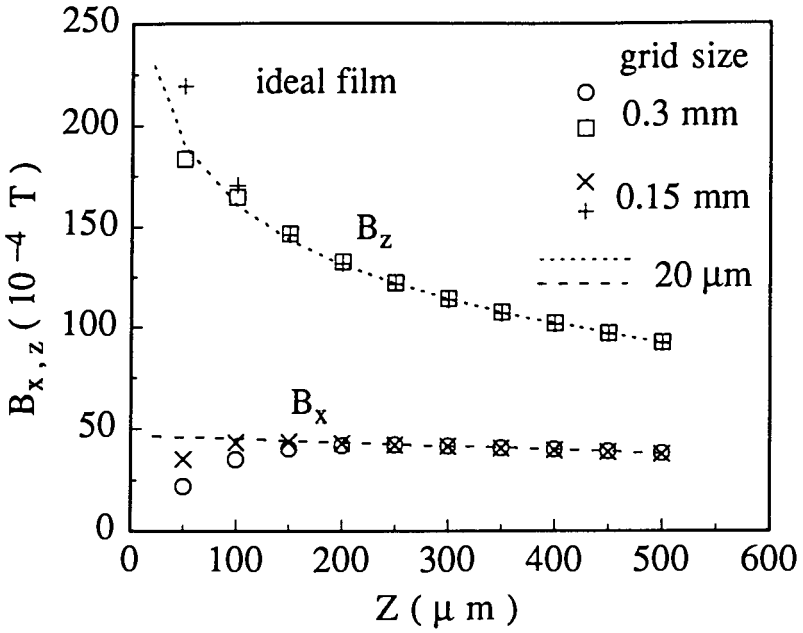

Fig. 4.2. Simulated B_x and B_z values versus z for different grid size w of the sheet magnetization M(x,y).

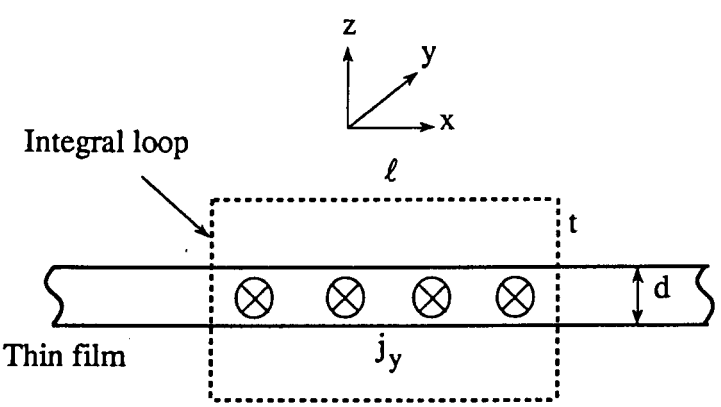

Fig. 4.3. Schematic diagram of the integral path of Ampere's law.

4.3. Results and discussion: General case

Figure 4.4 shows the measured maps of the magnetic flux density B_z by the scanning micro-Hall probe for sequentially applied external fields, $\mu_0 H_a$ = 2, 4, 6, 8, and 0 mT. The mapping of the magnetic flux density was carried out at a constant distance $z \approx 250$ μm above the film surface. The YBCO sample was maintained at 77 K during the flux mapping measurements.

The purpose of showing the B_z distributions for various applied fields ($\mu_0 H_a$ = 2, 4, 6, 8, and 0 mT), see Figs. 3.6 and 4.4, is to demonstrate the full extent of the magnetic vortex penetration in conjunction with calculations for the spatial distributions of the flux density **B**, as discussed below. The remanent flux mapping was carried out after the applied flux B_a = 8 mT was reduced to zero. In small applied fields, vortices are present only around the film edges, and the B_z map, see Fig. 4.4(a), shows no sign of sample defects. In medium applied fields, the vortices penetrate deeper into the film. The defect sites are now clearly visible, see Figs. 4.4(b)-(d). The critical sheet current is lower in those regions. The defect sites are also clearly visible for the remanent B_z map, see Fig. 4.4(e)

Figure 4.5 shows the magnetization maps M(x,y) and the sheet current distributions J(x,y) for various vortex states corresponding to those in Fig. 4.4. M(x,y) and J(x,y) were obtained by the inverse calculation procedure described in Chapter 3. Figure 4.5(a) shows that for $\mu_0 H_a$ = 2 mT, the magnetization surface and the current stream lines are very smooth. The shielding currents are nonzero but less than critical in the film interior. The current paths in these regions tend to become more and more rounded and eventually become circular when moving towards to the film center. For $\mu_0 H_a$ = 6 mT, sharp corners appear in the magnetization surface and that corresponds to rectangular current loops at the outer periphery of the film, see Fig. 4.5(c). In these regions, the induced

sheet current reached the critical value. Near the central part of the film, the rounding in current loop is still visible, and the current is less than critical.

Figure 4.6 shows distributions of the tangential components of **B** which were calculated by using Eq. (4.2) for the various vortex states shown in Fig. 4.4. Figures 4.6(a)-4.6(d) show that the B_x components of opposite signs are distributed over the two triangular regions which join in a common point in the center of the film. The development of the plateaus seen in the B_x maps corresponds to the evolution of the flux penetration, see Figs. 4.4 and 4.6. Figure 4.6(e) shows the remanent B_x distribution for an initially applied field $\mu_0 H_a = 8$ mT. The remanent case will be discussed latter.

Figure 4.6(f) shows the B_y component in an applied field of 6 mT. There are non-zero values of B_y over the region where B_x dominates, see Fig. 4.6(c). The appearance of B_y in this region is due to the presence of defects which are centered around (–3,0) and (3,0) in Fig. 4.4(c). Figure 4.5(c) shows that the current curves around these defects and that causes a simultaneous presence of the B_x and B_y components in that region. Note that in the absence of defects the components B_x and B_y appear in different triangular regions.

As discussed in Section 4.2.3, the profile of the tangential component B_x or B_y resembles the profile of the current distribution. The maps of the tangential flux densities B_x and B_y shown in Fig. 4.6 are equivalent to the maps of the sheet currents J_y and J_x. This can be seen more clearly by comparing the J_y and B_x as a function of x coordinate, see Figs. 3.7 and 4.7, for the same vortex states. Here both the $B_x(x)$ and $J_y(x)$ curves were plotted along a central line across the film ($y = 0$). The effect of the field-dependent critical currents in the thin-film superconductor is reflected in a gradual decrease of $B_{x,y}$ when the film edge is approached, see Fig. 4.6.

The visualization of the spatially distributed total magnetic flux density in the vicinity of the thin-film sample can be realized by vector field plots shown in Fig. 4.8 where the total flux density **B** was calculated by using Eq. 4.1 for the various vortex states, which correspond to those described in Figs. 4.1-4.7. The total flux density distribution was calculated in the x-z plane at y = 0, the central plane. The distribution height z above the film surface ranges from 0.2 to 5 mm. The lateral dimension of the **B** distribution extends from the center of the film (x = 0) to the outside of the film edge (x ≈ 7 mm). Thus, Fig. 4.8 provides a detailed and even more complete view of the evolution of the magnetic flux penetration and flux trapping.

Figures 4.8(a) and 4.8(b) show the saturation remanent flux distributions in the central x-z plane for the ideal and the YBCO films, respectively. These distribution patterns are very similar due to the similar sheet current distributions in the thin films, see Fig. 3.3. The sheet currents with the concentric square paths generate a maximum B_z at the film center and a minimum B_z at the film edge, in accordance with the observation in Fig. 3.4. The return flux (pointing in $-\hat{z}$ direction) due to the sheet currents is responsible for the demagnetizing effect around the film edges. The magnitude of **B** decreases rapidly away from the film surface. The distribution of the magnetic flux shows clearly the features which are typical to a dipole.

Figure 4.8(c) shows that for the weak applied field, $\mu_0 H_a$ = 2 mT, the induced supercurrents effectively shielded most of the region in the film from the external flux. However, the tangential components $B_{x,y}$ are present over the entire film surface, see Figs. 4.6(a), 4.7, and 4.8(c). According to Ampere's law, the screening currents are also present everywhere across the film including the vortex-free region. This is a good example demonstrating the close relationship between the sheet current and the tangential flux density in the thin-film

geometry. However, note that the values of $B_{x,y}$ in the vortex-free region are smaller than those in the vortex-penetrated regions where the supercurrent reached its critical value, see Figs. 4.6 and 4.7.

Figures 4.8(c)-4.8(f) demonstrate the evolution of the flux penetration as the applied field progressively increases, $\mu_0 H_a$ = 2, 4, 6, and 8 mT. The vortex front propagates towards the film center with an increasing applied field. Consequently, the vortex-free region where the flux lines appreciably deviate from the external field lines is more and more confined to the center of the film.

It is interesting to note that the perturbation of the external field by supercurrents occurs only within 5 mm above the film surface. This distance is approximately equal to the half length of the film edge, see for example Fig. 4.8(c).

Figure 4.8(g) shows the flux line patterns in a remanent state after the applied field $\mu_0 H_a$ = 8 mT was switched off. The sample was partially penetrated by the flux, see Fig. 4.4(e). The maximum B_z value corresponds to one of the four hilltops in the B_z map shown in Fig. 4.4(e). It is interesting to note that at the location of the B_z maximum, the tangential components $B_{x,y}$ vanish, and it follows that the sheet current also vanishes in this area. A close look at Figs. 4.4-4.5 showed that each local peak in the B_z map is encircled by sheet currents; at the point where B_z reaches maximum the current changes its sign and its magnitude goes through zero.

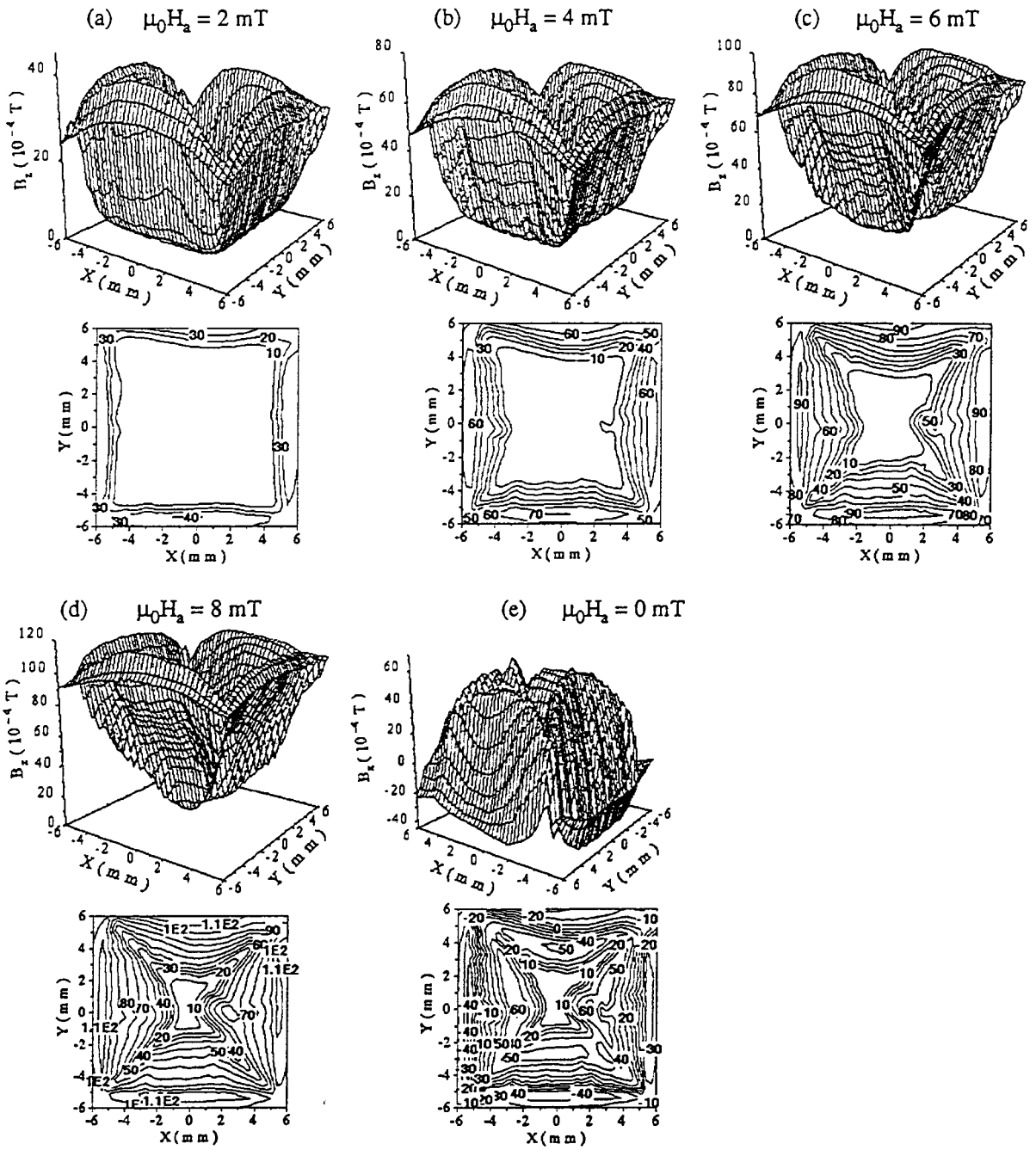

Fig. 4.4. Maps of B_z of the YBCO film measured by the scanning micro-Hall probe for different applied fields, $\mu_0 H_a$ = (a) 2, (b) 4, (c) 6, (d) 8, and (e) 0 mT.

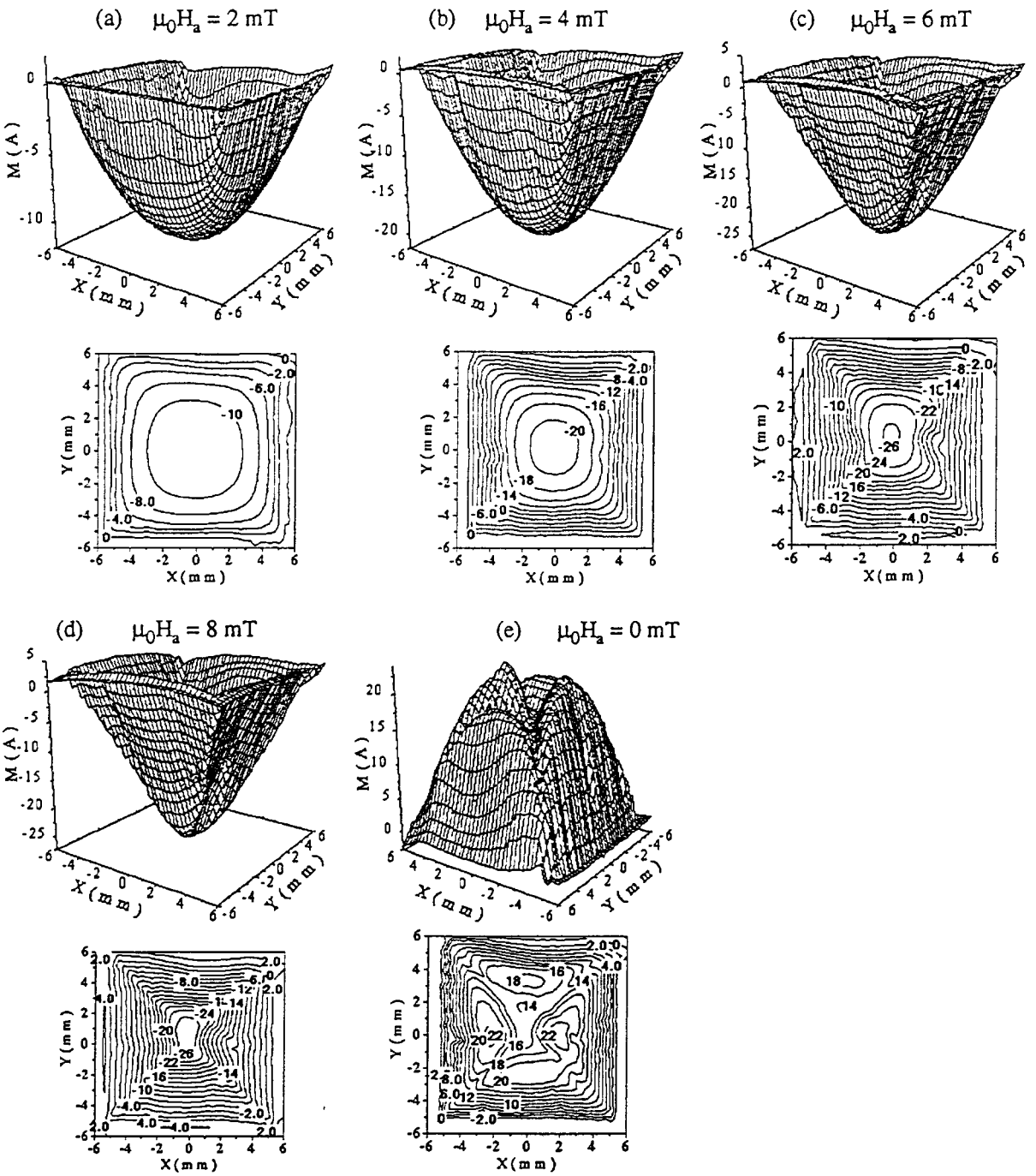

Fig. 4.5. The sheet magnetization M of the YBCO film for different applied fields, $\mu_0 H_a$ = (a) 2, (b) 4, (c) 6, (d) 8, and (e) 0 mT.

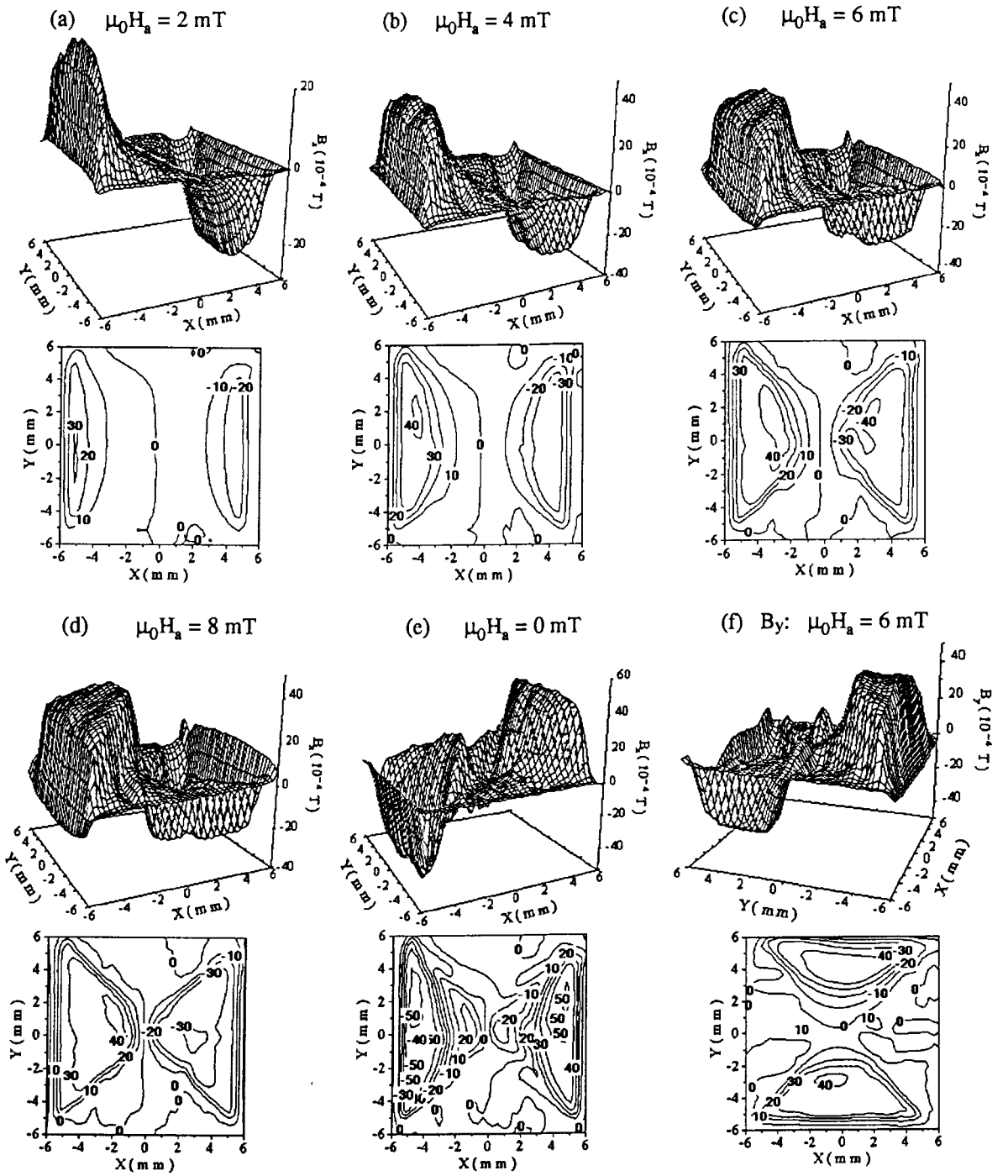

Fig. 4.6. $B_x(x,y)$ of the YBCO film for $\mu_0 H_a$ = (a) 2, (b) 4, (c) 6, (d) 8, and (e) 0 mT; (f) $B_y(x,y)$ for $\mu_0 H_a$ = 6 mT.

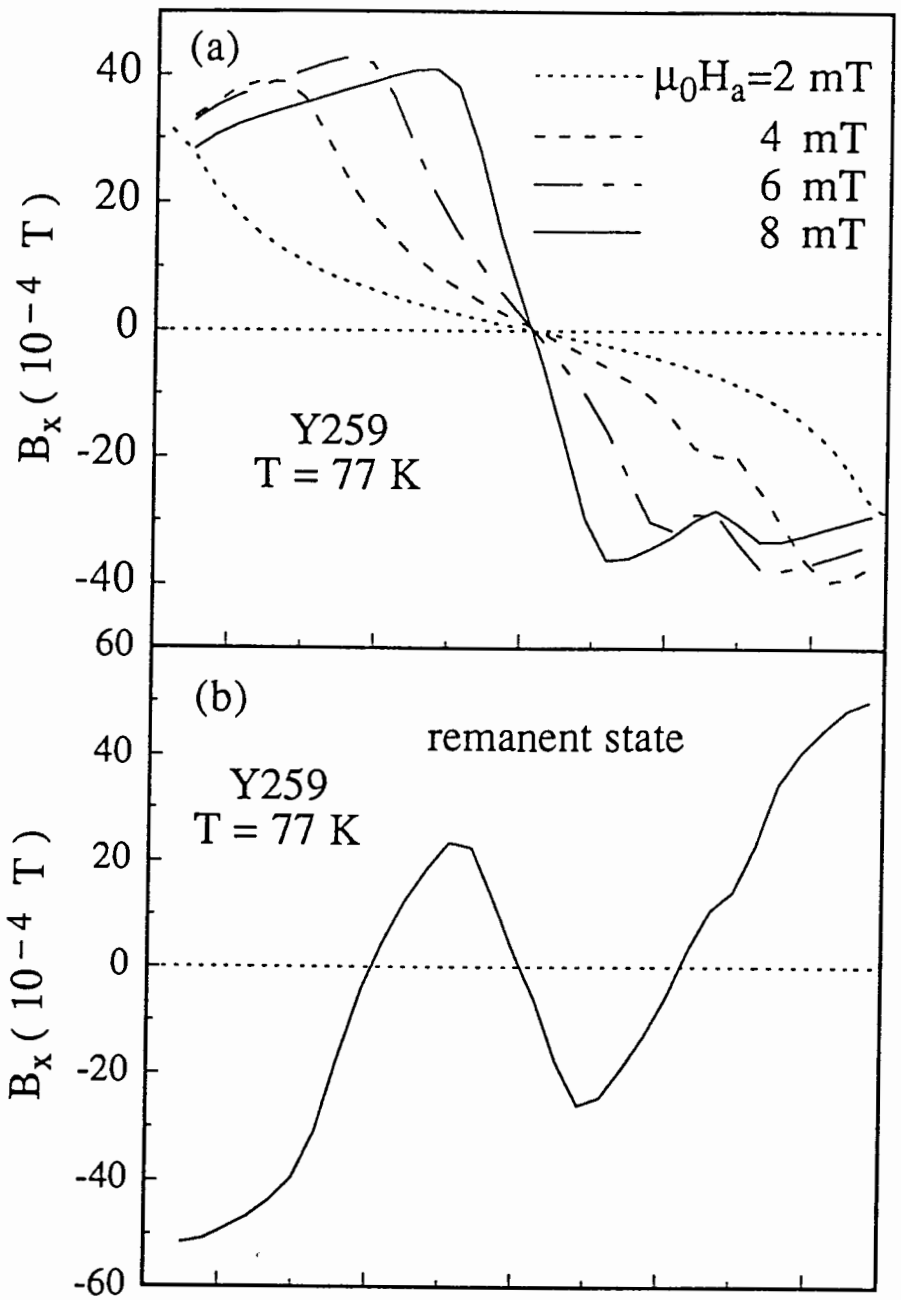

Fig. 4.7. B_x versus x for the YBCO film (a) in different applied fields; (b) in the remanent state.

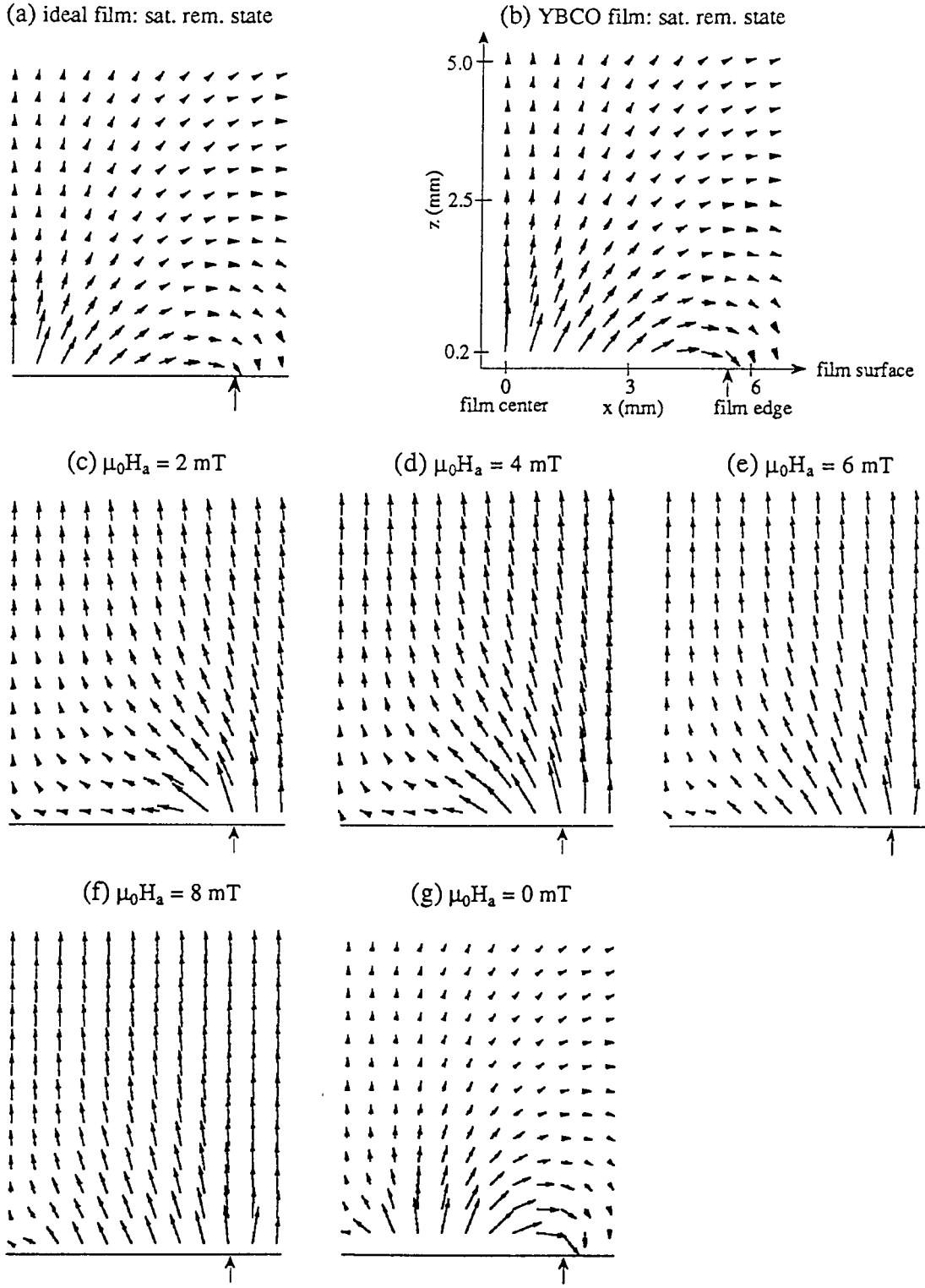

Fig. 4.8. Vector field plots of the total flux density **B** in the x-z plane (y = 0) in the saturation remanent state (a) and (b); and in different applied fields (for a YBCO film): $\mu_0 H_a$ = (c) 2, (d) 4, (e) 6, (f) 8, and (g) 0 mT.

4.4. Conclusions

We have shown in this chapter that the flux mapping by a scanning micro-Hall probe includes detailed and complete information about the spatial distribution of the total flux density **B** in the vicinity of a thin-film superconductor. The total flux density **B** is calculated from the sheet current which is evaluated from the sheet magnetization which was obtained by performing the inverse transformation described in Chapter 3. The spatial flux distribution includes both the normal component B_z and the tangential components $B_{x,y}$. The latter are not obtainable directly from our scanning micro-Hall probe measurements.

The minimum height z at which the tangential components $B_{x,y}$ is meaningful is determined by the scan step size w of micro-Hall probe measurements. The calculated normal component B_z, on the other hand, showed little dependence on w, due to the continuity of B_z across the film thickness.

For a thin-film superconductor with an applied field normal to the film surface, Ampere's law indicates that the induced sheet currents are nearly entirely determined by $2B_{x,y}/d$, where $B_{x,y}$ is the tangential flux densities at the film surface. Consequently, the values of $B_{x,y}$ at the sample surface can be obtained from the measured sheet currents.

The calculation of **B** in the vicinity of the film revealed several interesting features: (a) The tangential components $B_{x,y}$ are mostly present in separate and mutually perpendicular triangular regions. $B_{x,y}$ are nearly zero along the film diagonals. (b) A noticeable presence of B_x and B_y in the same region is a consequence of local defects. (c) The local maxima or minima of the normal flux density component B_z are encircled by circular current loops. The direction of supercurrents changes where B_z reaches its extremal values. At these points both the supercurrent sheet density and the in-plane B field go through zero. (d) The extent of the diamagnetic screening by supercurrents in the vertical direction is

comparable to that in the horizontal direction. With an increasing applied field, the flux penetrates deeper into the film and the vortex-free region is more and more confined to the center of the films.

Chapter 5
Conclusions

Studies of ac susceptibility and magnetic flux density mapping have been carried out in order to develop a better understanding of statics and dynamics of vortices in HTS thin films.

The ac susceptibility technique was found to be a simple and non-destructive method for characterizing HTS thin films. The best signal to noise ratio was achieved when the applied magnetic field H_a was oriented perpendicular to the film surface. The in- and out-of-phase components of the complex ac susceptibility, $\chi' - i\chi''$, were used to determine the transition temperature T_c and the critical current j_c as a function of temperature. $\chi' - i\chi''$ was found to be very sensitive to sample inhomogeneities, particularly in weak ac fields. Comparative studies were made between the measured and the calculated ac susceptibilities. The measured ac susceptibilities as a function of temperature and ac field showed good agreement with those calculated with a realistic distribution of sheet currents [Mikheenko and Kuzovlev 1993; Zhu et al. 1993; Clem and Sanchez 1994a]. The realistic approach predicts screening currents in the vortex-free regions. Our magnetic flux mapping measurements confirmed this prediction. The model calculations allowed us to evaluate the average critical current density j_c as a function of temperature from the ac susceptibility measurements. The j_c values determined by the ac susceptibility measurement are in fair agreement (within 20%) with those determined by the ac screening and flux mapping techniques.

The measurement of the flux penetration by means of the scanning Hall probe indicated that the peak in the out-of-phase component χ'', the maximum hysteretic loss, occurs when the magnetic flux penetrates nearly completely into the sample, i.e. ~ 100% flux penetration; a smaller flux penetration of ~ 70% was predicted

by the theoretical calculations [Mikheenko and Kuzovlev 1993; Zhu et al. 1993; Clem and Sanchez 1994a]. This discrepancy is mostly caused by field-dependent critical current densities in the measured samples as evidenced in the flux mapping studies.

The measured ac susceptibilities of the HTS films showed weak dependence on the ac driving frequency, f. This frequency dependence is attributed to the thermally activated flux creep of vortices which are driven into and out of the thin film during an ac cycle. It was observed that the $\chi''(T)$ peak temperature, T_p, shifts slightly to higher temperatures as the driving frequency increases. According to the Anderson-Kim flux creep model, this effect is equivalent to an increasing apparent screening current as the driving frequency f increases. The functional dependence of $T_p(f)$ was found to be well described by the scaling argument based on the flux creep theory. The typical activation barrier for a measured high quality YBCO thin film was estimated, $U \approx 0.16$ eV, at $T = 77$ K and for $\mu_0 H_a = 10^{-4}$ T. This activation barrier value is comparable to that obtained by other techniques, such as the flux noise measurement.

The scanning micro-Hall probe technique can be operated with a relatively high lateral resolution, does not influence the flux distribution, is quantitative, and is non-destructive. For homogeneous thin-film samples, the flux maps $B_z(x,y)$ demonstrated four-fold symmetric patterns that reflect the symmetry of the square geometry. The deviation of the symmetric pattern indicates the existence of defects or inhomogeneities.

The inverse calculation algorithm developed in this thesis allowed one to obtain the distribution of screening sheet currents from the measured flux map. It was found that the sheet currents are present over the entire thin-film sample, including the vortex-free region. In the vortex penetrated region the sheet current density reaches the critical value which was found to be field-dependent.

The critical sheet current follows the sample edges. This pattern of the critical current explains the unique behavior of the magnetic flux along the film diagonals: the flux trapping is enhanced in the remanent state and the flux screening (in the presence of an applied field) is more effective compared to other parts of the film. In the vortex-free region the sheet current value is less than the critical value. The sheet currents in this region have the tendency to avoid sharp turns and show complete circular loops when approaching the film center.

For a remanent state with partial flux penetration, four hill tops in the remanent $B_z(x,y)$ map were observed. Each hill top in the $B_z(x,y)$ map is associated with circulating sheet currents, resulting in multiply-connected current loops. Our studies showed that these complex flux and sheet current patterns can be reconstructed by the superposition of two virgin vortex states in the hysteretic cycle. This result implies the essential features of Bean's model (usually applied to the parallel field configuration) are also applicable to the square thin film geometry with the applied field perpendicular to the film surface.

The effect of the field-dependent critical current, even for the relatively low field values ($\mu_0 H_a < 12$ mT), was clearly evident in the Hall probe measurements. The local critical current was dependent on the local flux density. The field-dependent critical current density was found to follow the Kim model description.

The spatial distribution of the total flux density $\mathbf{B}(x,y,z)$, including the tangential components $B_x(x,y,z)$ and $B_y(x,y,z)$, was calculated in the vicinity of a thin-film sample from the known current distribution which was obtained by means of the inverse transform of the measured flux map $B_z(x,y,z_0)$, where z_0 is a fixed flux mapping height. The calculated B_x and B_y are mostly present in separate and mutually perpendicular triangular regions, compare Figs. 4.6(c)

with 4.6(f). The application of Ampere's law to the thin-film geometry showed that the sheet current is mainly governed by the curvature of **B** (= $2B_{x,y}/d$).

The total flux distribution allowed one to visualize the flux line patterns for different vortex states. The calculated flux lines around the HTS thin-film sample demonstrated the following features: (a) The flux lines show a dipole-like patterns. (b) The flux lines of the induced sheet currents always return around the film edges and lead to an enhancement of the flux density in this area, that profoundly affects the nucleation of vortices in high-T_c films. (c) In the presence of a weak applied field, the normal flux density is distributed only at the outer periphery of the film. The tangential flux density is distributed across the whole film surface. (d) The spatial extent of the diamagnetic effect in the vertical direction is comparable to that in the horizontal direction. (e) The flux front progressively propagates towards the film center as the magnitude of the applied field increases. This is indicated by the shrinking vortex-free region. (f) At the location where the normal flux density B_z shows a maximum (or minimum), the tangential flux densities $B_{x,y}$, and hence the sheet currents $J_{y,x}$, are zero.

The detailed studies about magnetic flux and current distributions have been very useful for the sample characterization of superconducting properties. The quantitative understanding of the vortex behavior in HTS thin films can help to control and to improve the relevant superconducting parameters of HTS films designated for device applications, such as flux pinning in low noise SQUID magnetometers operated at liquid nitrogen temperatures.

Appendix
The Integral of χ'' for the Realistic Approach

The integral (2.14b) is

$$I_{\chi''}(\eta) = \int_0^{\eta} U(x)dx, \tag{A1}$$

where U(x) is defined in (2.12b). It follows that

$$I_{\chi''}(\eta) = \frac{2}{\pi}\left[1 - \operatorname{sech}\eta + \eta\cos^{-1}(\operatorname{sech}\eta) - \int_0^{\eta} x\operatorname{sech}x\,dx\right]. \tag{A2}$$

The integral in the last term of (A2) cannot be solved analytically. Instead, it can be expressed by a polynomial,

$$\int_0^{\eta} x\operatorname{sech}x\,dx = \frac{\eta^2}{2} - \frac{\eta^4}{8} + \frac{5\eta^6}{144} + \cdots \frac{(-1)^n E_n \eta^{2n+2}}{(2n+2)(2n)!} + \cdots, \tag{A3}$$

where E_n is the Euler number

$$E_n = \frac{2^{2n+2}(2n)!}{\pi^{2n+1}}\left\{1 - \frac{1}{3^{2n+1}} + \frac{1}{5^{2n+1}} - \cdots\right\}. \tag{A4}$$

The first five Euler numbers are: $E_1 = 1$, $E_2 = 5$, $E_3 = 61$, $E_4 = 1385$, $E_5 = 50521$.

References

Anderson, P.W., **1962**, Phys. Rev. Lett. **9**, 309.

Anderson, P.W., and Y.B. Kim, **1964**, Rev. Mod. Phys. **36**, 39.

Asher, G.M., J.T. Williams, C.R. Walters, H. Joyce and R.J.A. Paul, **1982**, IEEE Trans. Magn. **18**, 540.

Atsarkin, V.A., G.A. Vasneva, and N.E. Noginova, **1992**, Superconductivity **5**, 417.

Bean, C. P., **1962**, Phys. Rev. Lett. **8**, 250.

Bean, C.P., **1964**, Rev. Mod. Phys. **36**, 31.

Blatter, G., M. V. Feigel'man, V. B. Geshkenbein, A. I. Larkin, and V. M. Vinokur, **1993**, Rev. Mod. Phys. **66**, 1125.

Brandt, E.H., M. Indenbom, and A. Forkl, **1993**, Europhys. Lett. **20**, 735.

Brown, P., **1994**, M.Sc. thesis, Simon Fraser University.

Brüll, P., D. Kirchgässner, and P. Leiderer, **1991**, Physica C **182**, 339.

Campbell, A.M., and J.E. Evetts, **1972**, Adv. Phys. **21**, 199.

Chen, D. X., and R. B. Goldfarb, **1989**, J. Appl. Phys. **66**, 2489.

Chen, D. X., J. Nogués, and K. V. Rao, **1989**, Cryogenics **29**, 800.

Chrzanowski, J., J. C. Irwin, B. Heinrich, A. E. Curzon, N. Fortier and A. Cragg, **1991**, Physica C **182**, 231.

Claassen, J. H., **1989**, IEEE Trans. Mag. **25**, 2233.

Claassen, J.H., M.E. Reeves, and R.J. Soulen, **1991**, Rev. Sci. Instrum. **62**, 996.

Claassen, J. H., **1992**, in: Magnetic Susceptibility of Superconductors and Other Spin Systems, R. A. Hein, T. L. Francavilla, and D. H. Liebenberg, eds., Plenum Press, New York, pp. 405-428.

Clem, J. R., **1988**, Physica C **153-155**, 50.

Clem, J.R., **1992**, in: Magnetic Susceptibility of Superconductors and Other Spin Systems, R.A. Hein, T.L. Francavilla, and D.H. Liebenberg, eds., Plenum Press, New York, pp. 177-211.

Clem, John R. and A. Sanchez, **1994a**, Phys. Rev. B **50**, 9355.

Clem, John R., **1994b**, to be published in the Proc. of the 7th int. workshop on critical currents in superconductors, Jan. 24-27, Alpbach, Austria.

CTF Systems Inc., 15-1750 McLean Avenue, Port Coquitlam, B.C., Canada V3C 1M9.

Däumling, M. and D. C. Larbalestier, **1989**, Phys. Rev. B **40**, 9350.

Ferrari, M.J., M. Johnson, F.C. Wellstood, J. Clarke, A. Inam, X.D. Wu, L. Nazar, and T. Venkatesan, **1989**, Nature **341**, 723.

Ferrari, M.J., M. Johnson, F.C. Wellstood, and J. Clarke, **1990**, Phys. Rev. B **64**, 72.

Fife, A.A., V. Angus, C. Backhouse, K. Betts, M.B. Burbunk, R.A. Cragg, K. Ferguson, F. Habib, P.R. Kubik, J. Nomura, M. Smith, P. Spear, J. Vrba, D. Wager, W. Westera, H. Zhou, B. Heinrich, J. Chrzanowski, J.C. Irwin, A.E. Curzon, S. Meng-Burany, S. Govorkov, P. Brown, and W. Xing, **1994a**, "Characterization of high T_c DC SQUID magnetometers", International workshop on high-temperature superconducting electron devices, Whistler, B.C., Canada.

Fife, A.A., G. Anderson, V. Angus, C. Backhouse, K. Betts, M.B. Burbunk, R.A. Cragg, K. Ferguson, F. Habib, P.R. Kubik, J. Nomura, M. Smith, P. Spear, W. Westera, H. Zhou, J. Vrba, B. Heinrich, A.E. Curzon, J.C. Irwin, J. Chrzanowski, S. Meng-Burany, S. Govorkov, P. Brown, and W. Xing, **1994b**, to be published in IEEE Trans. Appl. Supercon.

Frankel, D. J., **1979**, J. Appl. Phys. **50**, 5402.

Goldfarb, R. B. and J. V. Minervini, **1984**, Rev. Sci. Instrum. **55**, 761.

Goldfarb, R. B., **1986**, Cryogenics **26**, 621.

Goldfarb, R. B., A.F. Clark, A.I. Braginski, and A.J. Panson, **1987**, Cryogenics **27**, 475.

Goldfarb, R. B., M. Lelental, and C. A. Thompson, **1992**, in: Magnetic Susceptibility of Superconductors and Other Spin Systems, R. A. Hein, T. L. Francavilla, and D. H. Liebenberg, eds., Plenum Press, New York, pp. 49-80.

Gömöry, F. and P. Lobotka, **1988**, Solid State Commun. **66**, 645.

Grant, P.D., M.W. Denhoff, W. Xing, P.H. Brown, S. Govorkov, J.C. Irwin, B. Heinrich, H. Zhou, A.A. Fife, and A.R. Cragg, **1994**, Physica C **229**, 289.

Heinrich, B., S. Govorkov, J. Chrzanowski, P. Brown, J.C. Irwin, V. Angus, R.A. Cragg, A.A. Fife, and H. Zhou, **1994**, "Structural and magneto-optical studies of eptaxial YBCO films", 1st Canadian Applied Superconductivity Workshop, Oct. 14 & 15, 1994, Ottawa, Ontario, Canada.

Huebener, R.P., R.T. Kampwirth, and V.A. Rowe, **1969**, Phys. Lett. **30A**, 385.

Indenbom, M.V., V.I. Nikitenko, A.A. Polyanski, and V.K. Vlasko-Vlasov, **1990**, Cryogenics **30**, 747.

Ishida, T. and R. B. Goldfarb, **1990**, Phys. Rev. B **41**, 8937.

Jackson, J. D., **1975**, *Classical Electrodynamics*, (Wiley, New York), Chap. 5, pp. 132-168.

Keith, V. and H.J.T. Smith, **1993**, Physica C **218**, 8.

Kes, P.H., J. Aarts, J. van den Berg, C.J. van der Beek, and J.A. Mydosh, **1989**, Supercond. Sci. Technol. **1**, 242.

Kim, Y.B., C.F. Hempstead, and A.R. Strnad, **1962**, Phys. Rev. Lett. **9**, 306.

Kim, Y.B., **1964**, Rev. Mod. Phys. **36**, 39.

Malozemoff, A.P., T.K. Worthington, Y. Yeshurun, and F. Holtzberg, **1988**, Phys. Rev. B **38**, 7203.

Mikheenko, P.N. and Yu.E. Kuzovlev, **1993**, Physica C **204**, 229.

Murphy, S. D., K. Renouard, R. Crittenden, and S. M. Bhagat, **1989**, Solid State Commun. **69**, 367.

Nikolo, M., and R. B. Goldfarb, **1989**, Phys. Rev. B **39**, 6615.

Press, W.H., B.P. Flannery, S.A. Teukolsky, and W.T. Vetterling, **1985**, *Numerical Recipes: The Art of Scientific Computing*, (Cambridge University Press), Chap. 2, pp. 19-76.

Quantum Technology Corp., 1370 Alpha Lake Road, Unit 15, Whistler, B.C. Canada V0N 1B1, Telephone: (604) 938-0030.

Rauch, W., H. Behner, and E. Gornik, **1992**, Physica C **201**, 179.

Roth, B.J., N.G. Sepulveda, and J.P. Wikswo, **1989**, J. Appl. Phys. **65**, 361.

Rowe, V.A., R.P. Huebener, R.T. Kampwirth, **1971**, Phys. Status Solidi A **4**, 513.

Rusiecki, S. et al., **1990**, J. Less Com. Met. **164 & 165**, 31.

Scharen, M.J., A.H. Cardona, J.Z. Sun, L.C. Bourne, and J.R. Schrieffer, **1991**, Jpn. J. Appl. Phys., **30**, L15.

Senoussi, S., **1992**, J. Phys. III (France) **2**, 1041.

Shortley, G., and D. Williams, *Elements of Physics*, (Prentice-Hall, New Jersey, **1965**), Chap. 35, pp. 788-789.

Sun, J. Z., **1989**, Ph.D. Thesis, Chap. 5, pp. 97-139, Stanford University.

Sun, J. Z., M. J. Scharen, L. C. Bourne, and J. R. Schrieffer, **1991**, Phys. Rev. B **44**, 5275.

Tinkham, M., **1975**, *Introduction to Superconductivity*, (McGraw-Hill, New York), Chap. 4, 104-142.

Xing, W., **1990**, M.Sc. Thesis, Simon Fraser University.

Xing, W., B. Heinrich, J. Chrzanowski, J.C. Irwin, H. Zhou, A.R. Cragg, and A.A. Fife, **1993**, Physica C **205**, 311.

Xing, W., B. Heinrich, Hu Zhou, A.A. Fife, and A.R. Cragg, **1994a**, *J. Appl. Phys.*, **76**, 4244.

Xing, W., B. Heinrich, Hu Zhou, A.A. Fife, R.A. Cragg, and P.D. Grant, **1994b**, submitted to the Proc. of the 4th World Congress on Superconductivity, June 27-July 1, Orlando, Fla.

Xing, W., B. Heinrich, Hu Zhou, A.A. Fife, and R.A. Cragg, **1994c**, to be published in IEEE Trans. Appl. Supercon.

Zhu, J., J. Mester, J. Lockhart, and J. Turneaure, **1993**, Physica C **212**, 216.